

**Physically based correction of systematic errors of
Rotating Shadowband Irradiometers**

presented by

Anne Forstinger

Bachelor-Thesis in Physics
submitted to

Faculty for Mathematics, Computer Science and Natural sciences,
Department of Physics

of

RWTH Aachen
in September, 2018

Prof. Dr. rer. nat. Christopher Wiebusch, Institute III B, Experimental Physics

Dr. rer. nat. Stefan Wilbert, German Aerospace Center

Acknowledgements

First of all, I would like to thank Professor Wiebusch for the acceptance of this thesis.

Then, I would like to thank the Meteorology group of the German Aerospace Center in the city office in Almería for their support and welcoming work atmosphere. I thank especially Stefan Wilbert, head of the Meteorology group, for his support and help even during his vacations. It was a pleasure to work with the entire team.

In addition, I thank Fotovoltec, Solar Engineering for the supply of the measurements from Londrina and CSP Services in Almería for the communication with Fotovoltec.

I also thank Anton Driesse from PV Performance Labs for providing the measurement of the cosine dependence of the LI-COR LI-200SA.

For establishing and maintaining the Aeronet sites at Campo Grande SONDA, Gual Pahari, New Delhi and Tabernas I thank Enio B. Pereira, Gerrit de Leeuw, Philippe Goloub and Stefan Wilbert and their respective staff.

Personally, I would also like to thank my family and Martin for their support over the phone during my stay here in Spain and of course during my studies at the RWTH. It would not have been possible without them.

Table of Contents

ACKNOWLEDGEMENTS	2
TABLE OF CONTENTS	3
TABLE OF FIGURES	4
TABLE OF ABBREVIATIONS	5
1 INTRODUCTION	6
2 STATE OF THE ART	7
2.1 IRRADIANCE AND ATMOSPHERIC IRRADIANCE TRANSPORT MODELS	7
2.2 CONVENTIONAL MEASUREMENT OF IRRADIANCES	11
2.2.1 <i>Pyrheliometer</i>	12
2.2.2 <i>Thermopile pyranometers</i>	12
2.3 MEASUREMENT OF IRRADIANCES WITH ROTATING SHADOWBAND IRRADIOMETERS (RSIs)	12
2.3.1 <i>Existing Calibration and Correction Functions for RSIs</i>	15
3 DEVELOPMENT OF THE PHYSICAL CORRECTION AND CALIBRATION METHOD	19
3.1 BASIC CONCEPT OF THE PHYSICAL CORRECTION	19
3.1.1 <i>Simulation of the GHI, DHI and DNI spectra</i>	20
3.1.2 <i>Description of the combined spectral and temperature correction</i>	21
3.1.3 <i>Description of the new cosine correction</i>	24
3.2 CALIBRATION PROCEDURE	25
3.3 ESTIMATION OF THE SPECTRA FOR THE APPLICATION OF THE CORRECTION METHOD	26
3.4 SUMMARY	29
4 EXPERIMENTAL SETUP AND EVALUATION OF THE METHOD PERFORMANCE	29
4.1 MOTIVATION	30
4.2 MEASUREMENT SITES, USED SENSORS AND DATASETS	30
4.3 EVALUATION METHOD.....	31
4.4 PERFORMANCE WITH THE CALIBRATION FACTORS FROM THE PSA AT TWO LOCATIONS	31
4.4.1 <i>Correction results with different correction methods at NETRA, India</i>	31
4.4.2 <i>Correction results at Londrina, Brazil</i>	35
4.5 VARIABILITY OF THE CALIBRATION FACTORS AT THE PSA AND NETRA.....	38
4.6 SUMMARY	41
4.7 ROOM FOR IMPROVEMENT	41
4.7.1 <i>AOD and precipitable water vapor estimation at the PSA, Spain</i>	42
4.7.2 <i>AOD and precipitable water vapor estimation at NETRA, India</i>	45
4.7.3 <i>Summary of the options to improve the physical methods</i>	47
5 CONCLUSION AND OUTLOOK	48
APPENDIX	50
REFERENCES	56

Table of Figures

FIGURE 1: DETAILED SET-UP OF A MEASUREMENT STATION FOR GHI, DHI AND DNI WITH PYRANOMETERS AND A PYRHELIOMETER WITH AN AUTOMATED TRACKER AND A SHADOWBALL [DLR FROM (WILBERT ET AL., 2015), P. 41]	11
FIGURE 2: TWIN ROTATING SHADOWBAND IRRADIOMETER FROM CSP SERVICES IN RESTING POSITION.	13
FIGURE 3: SPECTRAL RESPONSES OF THE LI-COR 200 SENSOR FROM (LICOR, 2004) UNDER LABORATORY CONDITIONS (ASSUMED TO BE 25°C) AND THE GHI SPECTRUM UNDER G173, AIR MASS 1.5 ATMOSPHERIC CONDITIONS (ASTM, 2012)	14
FIGURE 4: AIR MASS BASED CORRECTION FUNCTION BY KING AND MYERS [REPRODUCED FROM (JESSEN ET AL., 2017), P. 9].....	16
FIGURE 5: CAT EAR CORRECTION BY AUGUSTYN ET AL. [REPRODUCED FROM (WILBERT ET AL., 2015), P. 27]	17
FIGURE 6: BASIC CONCEPT OF THE PHYSICAL CORRECTION	19
FIGURE 7: CALCULATED SPECTRAL RESPONSE OF THE LI-200 AT -30°C, 25°C AND 70°C AND THE GHI UNDER G173 AIR MASS 1.5 ATMOSPHERIC CONDITIONS.	22
FIGURE 8: SPECTRAL TEMPERATURE CORRECTION FACTOR $F_{\alpha F}$ IN COMPARISON WITH CURRENTLY USED BROADBAND TEMPERATURE CORRECTION FACTORS.....	24
FIGURE 9: ITERATION PROCESS OF THE CORRECTION METHOD FOR THE MOST ACCURATE ESTIMATION OF THE AOD WITH THE AVAILABLE DNI MEASUREMENT OF THE RSI.	28
FIGURE 10: ABSOLUTE BIAS AND RMSD OF CORRECTED MEASUREMENTS FROM NETRA WITH CALIBRATION FACTORS FROM THE PSA FOR THE GHI.	32
FIGURE 11: ABSOLUTE BIAS AND RMSD OF CORRECTED MEASUREMENTS FROM NETRA WITH CALIBRATION FACTORS FROM THE PSA FOR THE DNI.	33
FIGURE 12: ABSOLUTE BIAS AND RMSD OF CORRECTED MEASUREMENTS FROM NETRA WITH CALIBRATION FACTORS FROM THE PSA FOR THE DHI.....	34
FIGURE 13: ABSOLUTE BIAS AND RMSD OF CORRECTED MEASUREMENTS FROM LONDRINA WITH CALIBRATION FACTORS FROM THE PSA FOR THE GHI.	35
FIGURE 14: ABSOLUTE BIAS AND RMSD OF CORRECTED MEASUREMENTS FROM LONDRINA WITH CALIBRATION FACTORS FROM THE PSA FOR THE DNI.	36
FIGURE 15: ABSOLUTE BIAS AND RMSD OF CORRECTED MEASUREMENTS FROM LONDRINA WITH CALIBRATION FACTORS FROM THE PSA FOR THE DHI.....	37
FIGURE 16: CALIBRATION FACTORS FROM CALIBRATIONS AT THE PSA, SPAIN FOR DIFFERENT TIME RANGES AND THEIR RELATIVE DEVIATION WITH RESPECT TO THE LONGEST CALIBRATION TIME.....	39
FIGURE 17: CALIBRATION FACTORS OBTAINED AT NETRA, INDIA FOR DIFFERENT TIME RANGES AND CALIBRATION METHODS AND THEIR RELATIVE DEVIATION WITH RESPECT TO THE LONGEST CALIBRATION TIME.....	40
FIGURE 18: EVALUATION OF THE AOD CALCULATION BY (INEICHEN, 2008) AND CALCULATED PRECIPITABLE WATER VAPOR BY (GUEYMARD, 1993; GUEYMARD, 1995) FOR THE PSA, SPAIN.	43
FIGURE 19: EVALUATION OF τ_{550nm} FOR SUNNY TIME STAMPS OVER THE COURSE OF ONE YEAR AT THE PSA.....	44
FIGURE 20: EVALUATION OF τ_{550nm} FOR SUNNY TIME STAMPS BEFORE AND AFTER THE ITERATION AT THE PSA.	45
FIGURE 21: EVALUATION OF THE AOD CALCULATED BY (INEICHEN, 2008) AND CALCULATED PRECIPITABLE WATER VAPOR BY (GUEYMARD, 1993; GUEYMARD, 1995) FOR NETRA.	46
FIGURE 22: EVALUATION OF τ_{550nm} FOR SUNNY TIME STAMPS OVER THE COURSE OF ONE YEAR AT NETRA.....	47

Table of Abbreviations

Abbreviation	Meaning
Aeronet	aerosol robotic network
AM_{abs}	absolute air mass
AM_{alt}	altitude corrected air mass
AM_{rel}	relative air mass
α_1 and α_2	Angstroem exponents
AOD	aerosol optical depth
AOI	angle of incidence
β	Angstroem coefficient for turbidity
c-Si	crystalline silicon
Cert	calibration factor from the longest calibration time range
DHI	diffuse horizontal irradiance
DNI	direct normal irradiance
F_A	spectral response parameter or air mass correction (pre-existing)
F_B	cosine response parameter (pre-existing)
F_C	solar height or cat ear parameter
F_{cos}	cosine correction factor (newly developed)
F_α	temperature correction factor (pre-existing)
$F_{\alpha F}$	spectral temperature correction factor (newly developed)
Geu	correction and calibration functions as described by (Geuder, Pulvermüller, & Vorbrugg, 2008)
GHI	global horizontal irradiance
λ	wavelength
LI-COR constant	calibration factor provided by LI-COR Biosciences
p	Atmosphere pressure at ground level
QE	quantum efficiency; The yield of electrons per photon.
RSI	Rotating Shadowband Irradiometer
RSMD	root mean square deviation
Sedes2	enhanced model for cloud modification of irradiance spectra by (Myers, 2012; Nann & Riordan, 1991; S. Nann, 1990) altered according to (Jessen et al., 2018)
SMARTS 2.9.5	A Simple Model of the Atmospheric Radiative Transfer of Sunshine; simulation software for solar spectra on the earth's surface by (Gueymard, 1995; Gueymard, 2005); Desktop version 2.9.5
$SR(\lambda)$	spectral response as a function of wavelength
SZA	solar zenith angle
T_{LI}	Linke-Ineichen turbidity
τ_λ	AOD at wavelength λ
Vig	correction and calibration functions described by (Augustyn et al., 2004; King & Myers, 1997; Vignola, 2006)
WV	precipitable water vapor

1 Introduction

In the effort to produce more power with solar energy, solar plants are being built at different locations around the world. In order to qualify a location for a potential solar plant, it is important to know the available solar resources at the location as accurate as possible. The most accurate measurement stations for continuous measurements under well-maintained conditions consist of three thermopile sensors, that each measure either the direct normal irradiance (DNI), diffuse horizontal irradiance (DHI) or global horizontal irradiance (GHI). To reduce the effect of soiling, these sensors have to be cleaned daily in order to perform as desired (Jessen et al., 2017). While the measurement accuracy achieved by these measurement stations under well-maintained conditions is high, the cleaning and acquisition costs are a non-negligible cost factor. The cleaning costs are especially important when the desired location is very remote and impedes daily cleaning in many cases.

Rotating Shadowband Irradiometers (RSIs) measure all three irradiance components with one sensor that is less affected by soiling (Jessen et al., 2017). RSIs can therefore be deployed at remote locations with much lower maintenance costs. In addition, RSIs are cheaper than high accuracy stations because the used sensor is more inexpensive and no additional hardware is needed (Jessen et al., 2017 et al.; Licor, 2004). However, RSIs are in return not as accurate even under well maintained conditions with daily cleaning (Wilbert et al., 2015). The sensors that are built into the RSIs produce a non-uniform output signal. The magnitude of the output signal depends on the incoming spectrum, the sensor temperature and angle between the sensor surface and the incoming light.

All of these quantities induce errors in the measurement of the RSI and therefore reduce the accuracy of the RSIs. In order to remove these errors as far as possible, the RSIs measurements are corrected using correction functions. Current correction methods are developed solely on empirical relationships that were found at the respective development locations at which the RSI measurements were compared to thermopile sensor measurements. These corrections reduce the sensor temperature, the incidence angle and the spectral error of the RSI measurement. As soon as the sensor is deployed at a location with different climatic conditions, these empirical relationships might reach a lower accuracy than at the site at which they were developed. The remaining errors can be partly compensated by a site-specific calibration under atmospheric conditions that are similar to the ones expected during the measurement campaign. This is not always possible and implies additional costs. Calibration results obtained with a current calibration at a different site show a location dependence.

The new correction and calibration method, which is developed in this thesis, attempts to remove the measurement errors in the measurements using a physical method. It is based on information of the sensor properties and the atmospheric conditions at the measurement site. This way, no empirical relations obtained from a specific site are required. The method requires estimates of the current DHI and GHI spectra during each measurement of the sensor. Based on these spectra, a spectral correction, which includes a spectrum dependent temperature correction, can be made without employing empirical relationships.

2 State of the art

2.1 Irradiance and atmospheric irradiance transport models

Extraterrestrial solar radiation is the electromagnetic solar energy reaching the top of the earth's atmosphere. Sun light however, is only the visible part of the radiation (WMO, 2014). Radiation expressed in power per unit area is then defined as the irradiance. The solar irradiance at the earth's surface can be divided into three components. The global horizontal irradiance (GHI) is defined as the all irradiance that reaches a horizontally aligned surface from a solid angle of 2π . The diffuse horizontal irradiance (DHI) is defined as the all irradiance that reaches a horizontal surface from 2π solid angle but with the solid angle of the sun's disc screened out (WMO, 2014). Finally, the direct normal irradiance (DNI) can be defined as the direct irradiance from the solid angle of the sun's disk on a plane normal to the sun (WMO, 2014). These three components are connected by the following relationship [(Jessen et al., 2017), Eq. 2.1]:

$$DNI = \frac{GHI - DHI}{\cos SZA} \quad (1)$$

The SZA is the solar zenith angle and describes the sun's position. It is defined as the angle between the earth's surface normal and the position vector of the sun (Jessen et al., 2017). The here used GHI, DHI and DNI represent broadband values with the unit $\left[\frac{W}{m^2}\right]$.

Also, the spectral irradiances GHI_s , DHI_s and DNI_s are of interest. They have the unit $\left[\frac{W}{nm \cdot m^2}\right]$ and form the direct normal, diffuse horizontal and global horizontal solar spectra. Because broadband values are the spectra integrated over the wavelength, Eq. (1) applies to the spectra of GHI, DHI and DNI as well. The spectra of GHI, DHI and DNI are very different. Generally speaking, the DHI spectrum has more irradiance in the blue wavelength region and the DNI spectrum more irradiance in the yellow to red wavelength region compared to the other wavelength regions of the solar spectrum.

During the course of a day, the spectra change. This is the effect of extinction, which is both, scattering and absorption by molecules and particles in the atmosphere (WMO, 2014). Anyone can verify that the sky and sun have different colors at sun rise and sun set as opposed to the sky and the sun at mid-day. This is because in the early mornings and late evenings the distance, which the sun light travels through the atmosphere, is longer than at mid-day. This distance is quantified as the air mass. The relative air mass AM_{rel} is defined as the path length of air, AM_{abs} , through which the light travels from the current solar position to the observer with respect to the path through which the light travels at a SZA of 0° (Kasten & Young, 1989):

$$AM_{rel}(SZA) = \frac{AM_{abs}(SZA)}{AM_{abs}(0^\circ)} \quad (2)$$

The absolute air mass AM_{abs} is, amongst others, dependent on the air density at a specific height. Therefore, one can also define a relative pressure corrected air mass, which accounts for the variation in air density with pressure, and an altitude corrected air mass, which accounts for the height of a sensor above sea level (Kasten & Young, 1989).

The extinction of solar radiation in the atmosphere

How much of the sun light is absorbed or scattered on its way through the atmosphere depends on the gaseous and particle composition of the atmosphere. Especially, aerosols, which include dust, sea salt and smoke particles, that are present in the atmosphere can have a significant influence on the absorption and scattering of the solar irradiance (WMO, 2014). They therefore change the spectrum of the GHI, DHI and DNI as well.

The absorption and scattering of solar radiation by the atmosphere can be described by the aerosol optical depth (AOD). The AOD is defined as a measure for the distributed aerosols in the column of air between the sensor and the top of the atmosphere (Gueymard, 2005). This includes the extinction by pollutants as well as water vapor (WMO, 2014). Therefore, the AOD is dependent on the location and current weather.

The AOD is defined as a function of the wavelength of the incoming light. It changes strongly with the wavelength because, amongst others, the aerosols in the atmosphere have distinct absorption bands at different wavelengths. The AOD τ_λ is defined with the Angstroem coefficient for turbidity β and the Angstroem exponents α_1 and α_2 by (Gueymard, 2001):

$$\tau_\lambda = \beta_i \left(\frac{\lambda}{1000nm} \right)^{-\alpha_i} \quad (3)$$

α_1 is defined for wavelengths below 500nm and α_2 above this wavelength. β_i is β above 500nm and $2^{\alpha_2 - \alpha_1} \beta$ below 500nm. This is an attempt to account for the different spectral characteristics of aerosols at different wavelengths (Gueymard, 2001). With the Angstroem exponents, single scattering albedo and the asymmetry factor, which describe the scattering characteristics of the aerosol, the aerosol combination that is present in the atmosphere can be categorized into types, such as urban or rural (Gueymard, 1995).

Another significant impact on the solar spectrum has precipitable water vapor in the atmosphere. Water molecules have very distinct absorption bands in the solar spectrum (Gueymard, 2001). The precipitable water vapor is defined for the entire atmosphere column above the sensor and has the unit [cm] (WMO, 2014). It can either be measured by a sun radiometers (cf. below) or calculated with approximations derived by (Gueymard, 1993, 1994), using the ambient temperature and the relative humidity. The formulation is based on computed fit coefficients from empirical data and can be found in (Gueymard, 1993, 1994). A brief discussion is given in the following paragraph.

At first, the saturation vapor pressure E_S is calculated with the ambient temperature T_{amb} in Kelvin along:

$$E_S = \exp \left(22.329699 - 49.140396 \cdot \frac{100}{T_{amb}} - 10.921853 \cdot \left(\frac{100}{T_{amb}} \right)^2 - 0.39015156 \cdot \frac{T_{amb}}{100} \right)$$

This relationship is based on an extensive computational fit of a saturation data set by (Gueymard, 1993).

Then, a relative temperature coefficient that references the ambient temperature to 0°C (TT) is calculated:

$$TT = 1 + \left(\frac{T_{amb}}{273.15} \right)$$

The water vapor is now calculated with the relative humidity rh , the saturation vapor pressure and the relative temperature coefficient. The relationship is derived solely from an empirical data set:

$$WV = \frac{0.1 \cdot [0.4976 + 1.5265 \cdot TT + \exp(13.6897 \cdot TT - 14.9188 \cdot TT^3)] \cdot 216.7 \cdot E_S \cdot rh}{100 \cdot (T_{amb} + 273.15)} \quad (4)$$

With this relationship, it is possible to estimate the precipitable water vapor from the relative humidity and the ambient temperature. It is further discussed in section 4.7.

Simplification of the AOD

In order to simplify the AOD, (Ineichen & Perez, 2002) proposed the Linke-Ineichen turbidity T_{LI} , which essentially references the how many clean and dry atmospheres are needed in order to observe the current extinction. The formulation by (Ineichen & Perez, 2002) is air mass independent.

The Linke-Ineichen turbidity $T_{LI} > 2$ is calculated along the following equation [(Ineichen & Perez, 2002), Eq. 9]:

$$T_{LI} = \frac{\frac{1}{0.09} \cdot \log \left[\left(0.664 + \frac{0.163}{\exp\left(-\frac{alt}{8000m}\right)} \right) \cdot \frac{I_0}{DNI} \cdot \left(\frac{r_0}{r} \right)^2 \right]}{AM_{alt}} + 1 \quad (5)$$

With T_{LI} being the Linke-Ineichen turbidity, I_0 the solar constant, DNI the current direct normal irradiance, r_0 the mean distance and r the current distance between earth and sun, alt the altitude of the station and AM_{alt} the altitude corrected air mass.

For $T_{LI} < 2$ a correction is applied to account for the coherence between the GHI, DHI and DNI with an equation provided by (Ineichen & Perez, 2002), Appendix]:

$$T_{LI,cor} = T_{LI} - 0.25 \cdot (2 - T_{LI})^{0.5}, \text{ for } T_{LI} < 2 \quad (6)$$

(Ineichen, 2008) proposed the following the equation to convert the Linke-Ineichen turbidity to the current AOD at 550nm using precipitable water vapor and the current atmospheric pressure at ground level p :

$$\tau_{550nm} = \frac{T_{LI} - 0.376 \cdot \log(WV) - \left[2 + 0.54 \cdot \frac{p_0}{p} - 0.5 \cdot \left(\frac{p_0}{p} \right)^2 + 0.16 \cdot \left(\frac{p_0}{p} \right)^3 \right]}{3.91 \cdot e^{0.689 \cdot \frac{p_0}{p}}} \quad (7)$$

With T_{LI} being the Linke-Ineichen turbidity, WV the precipitable water vapor, $p_0 = 1013.15$ mbar normal pressure. This relationship is obtained by a fit from radiation transfer models and is further discussed in sections 4.7.1 and 4.7.2 for different locations.

Spectro radiometers

To know the exact spectral distribution of the three irradiance components, ground measurements with spectro radiometers have to be conducted. These sensors conduct measurements with a narrowband interference filter and a silicon based photodiode. They can be used for measurements of the AOD if no clouds are within a 10° angle of the sun and measurements of the precipitable water vapor in the atmosphere column above the sensor (WMO, 2014).

The Aeronet (aerosol robotic network) by the (NASA, August 2018) is one example of a network of spectro radiometers. It measures, amongst others, the Angstrom exponents, single scattering albedo and asymmetry factor at specific wavelengths (Dubovik & King, 2000). The broadband parameters of α_1 , α_2 , single scattering albedo and asymmetry factor can be calculated from these measurements as described by (Wilbert, 2014) at different locations around the world. Aeronet also provides historical data for some measurement sites as well as measurements of the ozone concentration and the precipitable water vapor (NASA, August 2018).

Atmospheric irradiance transport models

Since the Aeronet does not provide detailed atmosphere information for all desired locations, atmospheric irradiance transport models are developed. These radiative transfer calculations are based on different input parameters describing the atmospheric conditions. Gueymard developed such a model called A Simple Model of the Atmospheric Radiative Transfer of Sunshine (SMARTS 2.9.5) (Gueymard, 1995; Gueymard, 2005) that simulates the spectrum at the ground from a number of input parameters. The input parameters that are used to model the needed spectra in this thesis are the following (Gueymard, 2005):

- the pressure
- the atmosphere type as defined by the temperature, season, relative humidity, and average daily temperature
- the precipitable water vapor
- the ozone concentration
- the CO₂ concentration
- the aerosol type (α_1 , α_2 , single scattering albedo and asymmetry factor)
- the turbidity (either τ_{550nm} or β)
- the sun-earth distance and the extraterrestrial solar spectrum
- the non-pressure corrected air mass
- the albedo of the sensor's surroundings

From these input parameters, SMARTS 2.9.5 is able to simulate the GHI, DHI and DNI spectra at the earth's surface for a cloudless sky.

Clouds affect the spectra of the irradiance components, in very different measures. A cloud in front of the sun for instance, affects the DNI heavily. The magnitude of the effect depends on the cloud's nature. A cloud, however, that is not directly in front of the sun doesn't only affect the GHI and DHI, but also the

DNI. The irradiance might be lessened through absorption or even increased by reflections between clouds and the ground (Nann & Riordan, 1991).

As described above clouds have various impacts on the examined spectra. Nann and Riordan developed an empirical model, called Sedes2 to account for the impact of clouds on the spectrum (Nann & Riordan, 1991; S. Nann, 1990). The model assumes that clouds act as grey filters on the spectra, and change the irradiance distribution across the wavelengths through scattering mechanisms. The model derives a clearness index based on the GHI broadband measurement and the extraterrestrial irradiance. The clearness parameter is then used to calculate a cloud cover modifier. This modifier is an empirical relationship developed with data from Stuttgart, Germany (Nann & Riordan, 1991; S. Nann, 1990).

Input parameters include the precipitable water vapor, the solar geometry, the DHI and the GHI. The output is the cloud modified spectrum of the GTI (global tilted irradiance) (Nann & Riordan, 1991). (Myers, 2012) altered the original algorithm for the processing of hourly broadband global, diffuse and direct irradiance to their corresponding spectra. Sedes2 was also enhanced to use the local standard time and calculates the solar position with subroutines from (Michalsky, 1988; Wilcox & Marion, 2008). The here used algorithm is altered in such a way that the spectra of the GHI and DNI are cloud modified (Jessen et al., 2018).

The following section 2.2 describes the measurement of the broadband irradiance components GHI, DHI and DNI.

2.2 Conventional measurement of irradiances

The three irradiance components are conventionally measured with thermopile sensors.

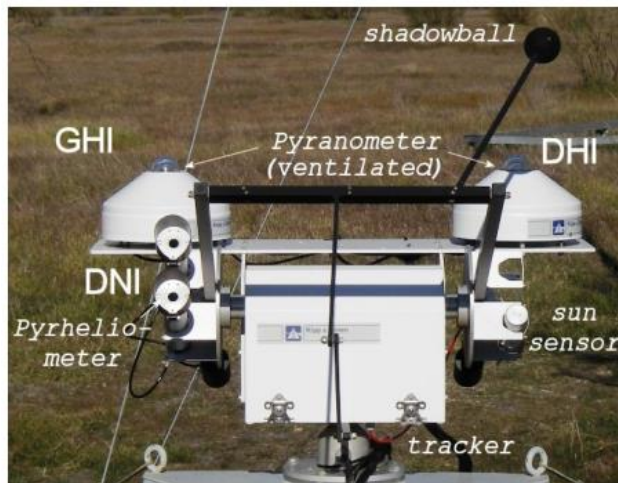


Figure 1: Detailed set-up of a measurement station for GHI, DHI and DNI with two pyranometers and a pyr heliometer with an automated tracker and a shadowball [DLR from (Wilbert et al., 2015), p. 41].

These are based on a serial circuit of thermocouples, which consist of wires of different materials. When light falls onto the sensor, it warms an absorber coating, which covers one of the surfaces of the disk-shaped thermopile. The temperature difference induces an electric potential into the thermopile, which is then proportional to the solar flux. Because of the set-up, the response time is relatively low, about 1-5s, but the measurement does not depend on the incoming spectrum (Jessen et al., 2017). Figure 1 displays the detailed set up of the sensors for a conventional measurement station. It consists of two sensors for the GHI and DHI, which are measured with pyranometers and one sensor for the DNI, which is measured with a pyr-heliometer. The pyr-heliometer is deployed on

a sun tracker that also utilizes a shadowball for the measurement of the DHI. The tracker operates with a sun sensor, which is also displayed in Figure 1. The following two sections 2.2.1 and 2.2.2 explain the deployment of thermopile sensors to measure the irradiance components GHI, DHI and DNI.

2.2.1 Pyrheliometer

A pyrheliometer is a thermopile sensor that measures the DNI. The thermopile sensor is built into a tube that shades the sensor from any light that does not fall directly into tube. An example of a pyrheliometer is displayed in Figure 1. The entire sensor is then aligned with the sun by a solar tracker (cf. Figure 1). This way, it is ensured that only the irradiance coming from the solid angle of the sun's disk, which is the definition of the DNI, is measured. Pyrheliometers that are deployed in the field are covered with a window to shield the sensor from dirt. For this reason, they have to be cleaned regularly.

2.2.2 Thermopile pyranometers

The GHI and DHI are measured with pyranometers. Thermopile pyranometers consist of thermopile sensors that are shielded from dirt and wind by a glass dome. For both, the measurement of the GHI and DHI, the pyranometers have to be aligned exactly horizontally. This ensures that all available radiation from a 2π solid angle reaches the sensor and can be measured. For the measurement of the DHI, however, the sun is blocked out by a shadow ball. This is a tracked shading device that will block out any radiation from the solid angle of the sun's disk. That way, the measurement of the DHI includes solely the radiation that does not come directly from the sun (Jessen et al., 2017). An automated tracker for the shadow ball is needed and can be seen in Figure 1. Both pyranometers are ventilated in order to reduce unwanted temperature effects on the measurements.

2.3 Measurement of irradiances with Rotating Shadowband Irradiometers

Although the measurements carried out with a solar tracker and thermopile sensors are very accurate under well-maintained conditions, the initial costs are very high because of the needed auxiliary devices. When deploying the pyranometers outside, a layer of dust and other forms of dirt will collect on the glass dome. This heavily impairs the measurement of the thermopile sensor because the light is damped through the layer of dirt. For this reason, pyrheliometers and pyranometers have to be cleaned daily, which increases the maintenance costs (Jessen et al., 2017).

The soiling effect is most noticeable for the pyrheliometers as the opening angle defined by the sensor element and the entrance window is quite small (2.5°) and even forward scattering by dust particles reduces the DNI measurement strongly (Jessen et al., 2017). Due to these shortcomings of thermopile measurements Rotating Shadowband Irradiometers (RSIs) were developed. RSIs determine all three irradiance components with one sensor. The used sensor is a silicon pyranometer. In Figure 2 the general appearance of a Twin RSI by CSP Services can be seen as deployed at the PSA, Spain. Twin RSIs use two sensors as opposed to one, but the general measurement is the same for RSIs and Twin RSIs.



Figure 2: Twin Rotating Shadowband Irradiometer by CSP Services in resting position. The two Si pyranometers are indicated as well as the shadowband.

The Twin RSI uses two silicon pyranometers as measurement sensors, which are displayed in Figure 2. A shadowband, which is displayed in Figure 2 in the resting position, rotates 360° around the silicon pyranometers. The measurement principle is as follows: First, the sensor measures the GHI, unshaded, while the shadowband is pointing towards the ground, just like in Figure 2. Once every minute, a shadow band rotates around the sensor. As soon as this rotation starts, the frequency of measurement recording is increased. Because the shadowband rotates 360° around the sensor, it will shade the sun at one point during the rotation. From that measurement burst, the DHI can be deducted as the lowest measurement value. The DNI can then be calculated along Eq. (1) from the GHI and DHI measurements (Jessen et al., 2017). The used sensor is less impaired by soiling because of its measurement technique (Wilbert et al., 2015).

Therefore, the RSI can be deployed at remote locations solely with a solar panel as power source and little additional maintenance is required. This aspect as well as the fact that only one sensor and no additional equipment such as a tracker is needed, reduces the cost of such a measurement station significantly (Wilbert et al., 2015).

One downside of the RSI is its silicon-based sensor, which is essentially a photodiode. It can therefore only measure wavelengths from about 400nm to 1100nm (Licor, 2004) and the sensors responsivity to each wavelength of incoming light is not uniform. The response of the sensor, however, is within microseconds. Its output is the short circuit, which is proportional to the portion of the incoming radiation that is converted to electrical energy (Vignola et al., 2016).

Due to the inhomogeneous spectral response of the photodiode, the measurement of the RSI is dependent on the spectrum under which it is operated. This is referred to as the spectral error. The inhomogeneous spectral response is illustrated in Figure 3 as well as the GHI spectrum for G173 atmospheric conditions and air mass 1.5 (ASTM, 2012). The spectral response curve is provided by (Licor, 2004). It is assumed that this spectral response was measured at 25°C because that is the standard temperature for laboratory conditions.

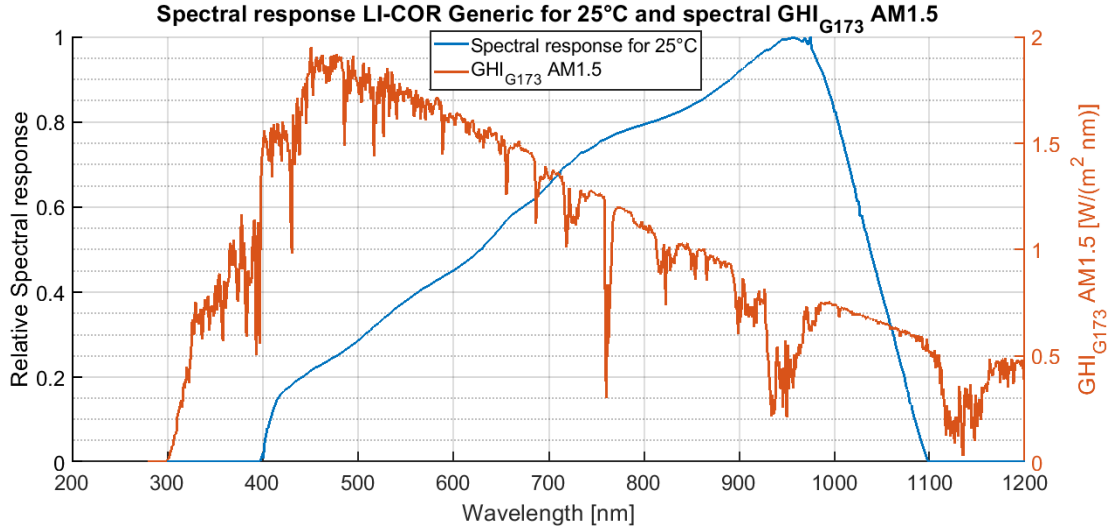


Figure 3: Spectral response of the LI- 200 sensor from (Licor, 2004) under laboratory conditions (assumed to be 25°C) and the GHI spectrum under G173, air mass 1.5 atmospheric conditions (ASTM, 2012).

The average responsivity, which references the short circuit to the broadband irradiance of the incoming spectrum, of the pyranometer is defined as

$$R_{ave} = \frac{\int d\lambda SR(\lambda) \cdot I_s}{\int d\lambda I_s} \quad (8)$$

Here, the spectral response $SR(\lambda)$ is defined as the size of the output signal relative to the highest signal and I_s is the spectrum under which is sensor is operated (Vignola et al., 2016).

The spectral response of a crystalline silicon (c-Si) photovoltaic sensor is dependent on the temperature because of the temperature dependency of the indirect band gap of c-Si (King-Smith, 1989). This stems from an increased electron-phonon coupling (Bludau, 1974; King-Smith, 1989). Phonons are defined as the lattice vibrations of the crystal (Klingshirn, 2006). When the temperature increases, the phonon energy as well as the electron-phonon coupling increases and the electrons then can overcome the indirect band gap at lower photon energies (Rajkanan, Singh, & Shewchun, 1979)[(Varshni, 1967), p.7]. This corresponds to longer wavelengths of the incoming light.

Near the absorption edge of the indirect band gap of silicon of 1.1557eV or 1073nm this effect is most dominant (Rajkanan et al., 1979). This leads to an increased yield of electrons per photon at higher temperatures at long wavelengths. The yield of electrons per photons is defined as quantum efficiency QE . Therefore, the spectral response, which is proportional to the quantum efficiency of the device (Hishikawa et al., 2018), is increased for long wavelengths and high temperatures especially near 1073nm. However, this is only an examination of pure silicon and can change when dealing with actual photovoltaic devices due to impurities and lattice deformations of the crystal [(Varshni, 1967), pp.1-2]. The measurement of the RSI is therefore also affected by a temperature error. As explained above, for the silicon based photodiode the spectral and temperature error are intervened.

(Hishikawa et al., 2018) developed a model for c-Si based photovoltaic devices, which is based on a wavelength dependent temperature shift of the quantum efficiency. In this thesis, that model is applied to the quantum efficiency of the RSI sensor for the first time. The model as well as its application for this specific case is discussed in detail in section 3.1.2.

The used silicon pyranometer is covered with an acrylic diffuser head (Licor, 2004). The shape and the physical properties of the diffuser define the sensor sensitivity on the angle of incidence. The dependence is not perfectly following a cosine, which is expected for a perfect black body. The cylinder-shaped diffuser allows irradiance to enter through the top of the cylinder as well as through the sides. This compensates that at very low AOIs, the transmittance of the cylinder top is also very low. One reason for that is that a bigger portion of the irradiance is reflected at the top of the cylinder. However, some deviations from the cosine dependence still occur. This is referred to as the cosine dependence of the sensor.

2.3.1 Existing Calibration and Correction Functions for RSIs

The following two sections explain the currently available calibration and correction functions that are based on empirical relationships for RSIs with LI-200 sensors (Wilko Jessen, 2017).

King, Myers, Augustyn and Vignola

The correction functions described by (Augustyn et al., 2004; King & Myers, 1997; Vignola, 2006), in the following referred to as Vignola, are based on a GHI correction on the grounds of the following empirical formula [(Jessen et al., 2017), Eq. 3.1]:

$$GHI_{corr} = GHI_{raw} \cdot \frac{F_{\alpha}}{F_A F_B F_C} \quad (9)$$

With GHI_{raw} being the uncorrected measured GHI, F_{α} the temperature correction factor, F_A the spectral response parameter, F_B the cosine response parameter and F_C the solar height or cat ear parameter.

The temperature correction factor is a broadband linear temperature correction, formulated by (King & Myers, 1997):

$$F_{\alpha} = 1 - \alpha_K \cdot (T_{RSI} - T_{ref}) \quad (10)$$

The slope was derived by measuring seven different LI-COR sensors at different temperatures following a standard procedure for photovoltaic reference cells. α_K is determined to be $8.2 \cdot 10^{-4} 1/K$ (King & Myers, 1997).

The spectral response correction or air mass correction F_A is a cubic function of the absolute air mass derived by (King & Myers, 1997) for clear sky conditions. Clear sky in this context means no clouds are present at the sky. The function only uses the change of the spectrum with the change of air mass and was obtained by a fit through the measurements displayed in Figure 4. The obtained formula by (King & Myers, 1997) is:

$$F_A = 2.631 \cdot 10^{-4} \cdot AM_{abs}^3 - 6.319 \cdot 10^{-3} \cdot AM_{abs}^2 + 5.401 \cdot 10^{-2} \cdot AM_{abs} + 0.932 \quad (11)$$

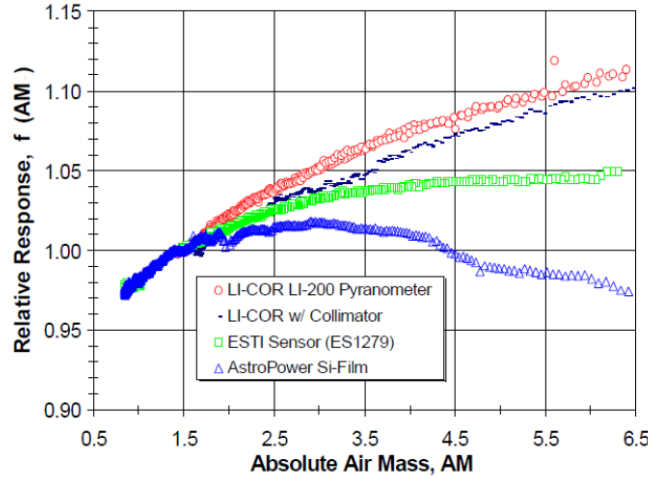


Figure 4: Air mass based correction function by King and Myers [reproduced from (Jessen et al., 2017), p. 9]

The sensor, that is used in a RSI, is covered with an acrylic diffusor head that only cosine corrected up to 80° SZA (Licor, 2004). For this effect, the cosine correction function F_B is developed by (King & Myers, 1997) and the cat ear correction F_C (cf. below) is developed by (Augustyn et al., 2004).

F_B corrects the sensor's response to different solar zenith angles and is cubic in the SZA [(Jessen et al., 2017), Eq. 3.5]:

$$F_B = -4.504 \cdot 10^{-7} \cdot SZA^3 + 1.357 \cdot 10^{-5} SZA^2 + 6.074 \cdot 10^{-4} \cdot SZA + 1 \quad (12)$$

This function is derived in an outdoor test by (King & Myers, 1997). For this, the sensor is mounted on a tracker and the response at different SZA is measured by moving the sensor to pre-defined angles. Even though the outdoor parameters like the absolute irradiance, the spectra and the ambient temperature were kept constant during the measurement [(King & Myers, 1997), p. 5], the obtained function is still dependent on the air mass correction function F_A . For this reason it is not possible to apply the cosine correction function on its own to the GHI. The data was also only acquired up to 80° SZA and was extrapolated to 90° SZA.

(Augustyn et al., 2004) derived an additional angle correction called the "cat ear correction". It accounts for an increased sensor response at solar zenith angles above 75° because of the sensor geometry, which is not covered by the extrapolated cosine correction function. Figure 5 displays the cat ear correction as published by (Augustyn et al., 2004). The corresponding equation for calculating the cat ear correction is [(Augustyn et al., 2004), Eq. 4 and 5, p. 3]:

$$F_C = \begin{cases} 10.16 + 0.001603 \cdot SZA^2 - 0.2424 \cdot SZA & \text{for } 75^\circ < SZA < 81^\circ \\ -58.03442 + 1.457577 \cdot SZA - 8.99 \cdot 10^{-3} \cdot SZA^2 & \text{for } 81^\circ \leq SZA < 83.2^\circ \\ 1 & \text{for } 0^\circ \leq SZA < 75^\circ \text{ or } SZA \leq 83.2^\circ \end{cases} \quad (13)$$

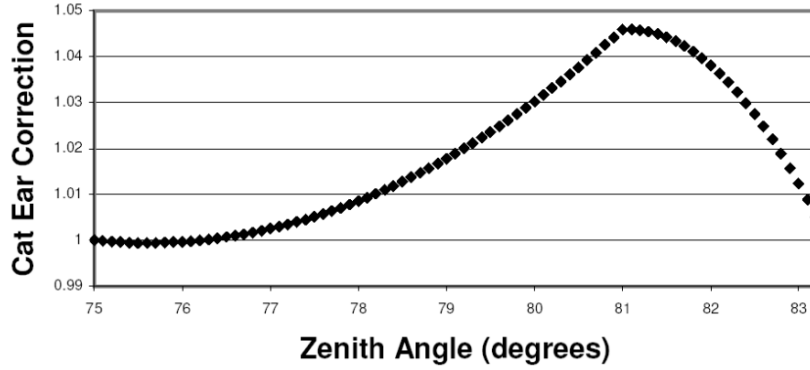


Figure 5: Cat ear correction by Augustyn et al. [reproduced from (Wilbert et al., 2015), p. 27]

(Augustyn et al., 2004) derived this function after all corrections described above were applied to the measurements. This means again that it is only possible to apply this function in combination with F_A and F_B .

Finally, a DHI correction is made using the fully corrected GHI according to Eq. (9). This correction is necessary because the spectral distribution of the DHI is fundamentally different from the GHI. It has more irradiance in the blue region of the spectrum as opposed to the GHI (cf. section 2.1). The used sensor is less sensitive in that region of the spectrum (cf. Figure 3), which is why (Vignola, 2006) proposed a DHI correction. The equations are derived with empirical measurements from Eugene, Oregon and are defined as the following (Vignola, 2006) [(Jessen et al., 2017), Eq. 3.7 and 3.8]:

$$\text{For } GHI_{cor} \leq 865.2 \frac{W}{m^2}$$

$$DHI_{cor} = DHI_{raw} + GHI_{cor} \cdot (-9.1 \cdot 10^{-11} \cdot GHI_{cor}^3 + 2.3978 \cdot 10^{-7} \cdot GHI_{cor}^2 - 2.3133 \cdot 10^{-4} \cdot GHI_{cor} + 0.1107)$$

$$\text{For } GHI_{cor} > 865.2 \frac{W}{m^2}$$

$$DHI_{cor} = DHI_{raw} + GHI_{cor} \cdot (0.0359 - 5.54 \cdot 10^{-6} \cdot GHI_{cor}). \quad (14)$$

This set of correction factors is used to correct the GHI and DHI measurements of the RSI.

Calibration procedure for RSIs with corrections from (Vignola, 2006)

This set of correction factors is used to correct the GHI and DHI measurement of the RSI. The calibration procedure is that the RSI is first deployed at a calibration station with a nearby reference station equipped with thermopile sensors measuring DNI, GHI and DHI.

After the data acquisition and proper filtering of the raw data, the LI-COR constant is applied to all measurements of the RSI. This is a calibration factor provided by LI-COR Biosciences, the manufacturer of the used sensor (Licor, 2004). This calibration is a coarse calibration with 5% uncertainty that is not accurate enough for the field deployment of the RSI (Jessen et al., 2017)..

Then, the correction functions are applied as described above. Then, the calibration factor of the GHI is obtained by minimizing the root mean square deviation (RMSD) of the corrected GHI and the reference GHI. The corrected GHI is then multiplied with the obtained calibration factor. The result is used as the GHI for all further calculations. Then, the DHI is corrected along Eq. (14) using the previously calculated GHI. The corrected DHI is multiplied by the calibration factor for the DHI which is determined using a RMSD minimization of the corrected DHI and the reference DHI. Finally, a calibration factor for the DNI is calculated with an RMSD minimization of the calculated DNI from the RSI and the reference DNI. The calculated DNI is obtained by employing Eq. (1) and using the GHI and DHI that are fully corrected and multiplied with their respective calibration factors. DNI is then multiplied with its calibration factor (Jessen et al., 2017).

The result is a set of three calibration factors for GHI, DHI and DNI, respectively. When the RSI is deployed at any location, the measurements of the three components are corrected like the following. First, the GHI is corrected and then multiplied with the GHI calibration factor. Then, the DHI is corrected, using the fully corrected GHI, and the DHI calibration factor is applied. Then, the DNI is calculated from the fully corrected GHI and DHI and the DNI calibration factor is applied. The results are improved measurements of the RSI (Jessen et al., 2017).

To compensate remaining spectral and cosine errors, the minimum calibration time for a RSI is one month although two months are recommended (Jessen et al., 2017).

DLR2008 (Geuder et al., 2008)

Another set of calibration and correction functions is published by (Geuder et al., 2008). The used functions are proprietary and are therefore not presented completely in this thesis.

First, a temperature correction is applied as well according to Eq. (10), but with a different slope α . The difference stems from a different measurement conducted by (Geuder et al., 2008) and was derived as $\alpha_G = 7 \cdot 10^{-4} \text{ 1/K}$. The measurement procedure is described later in more detail when comparing it to a correction function derived within this thesis (see section 3.1.2).

Then, (Geuder et al., 2008) uses a DHI spectral correction parameter, which is calculated from the broadband GHI, DHI and DNI to account for underestimations especially for deep blue skies. This spectral correction parameter is also dependent on the ambient temperature. The GHI is then corrected with a combination of the cat ear and angle of incidence correction, which also accounts for spectral effects (Jessen et al., 2017).

At last, the DHI and DNI are corrected by cubic and linear correction functions depending on the intensities of the irradiances (Jessen et al., 2017).

Calibration procedure by Geuder

The calibration and correction procedure is the same as described for Vignola (c.f. above). The main difference is that (Geuder et al., 2008) only use two calibration factors, one for the GHI and one for the DHI. The calibration factor for the DHI is calculated with an RMSD minimization of the corrected DHI and

the reference DHI. To obtain the GHI calibration factor, also a RMSD minimization is done, but with respect to the reference DNI. The DNI is calculated with the corrected DHI applied with the already determined DHI calibration factor and the corrected GHI applied with a variable GHI calibration factor for the RMSD minimization. The RMSD of the calculated DNI and the reference DNI is minimized by varying the GHI calibration factor. The advantage of this method is, that only two calibration factors are needed and the relationship between the GHI, DHI and DNI is fully exploited (Jessen et al., 2017). The calibration duration is similar to the Vignola calibration, one month minimum, but two months are recommended (Jessen et al., 2017).

In the field, the obtained calibration factor for the GHI is applied first to the corrected GHI, then the DHI is corrected and the DHI calibration factor is applied. The DNI is then calculated from the fully corrected GHI and DHI (Jessen et al., 2017).

3 Development of the physical correction and calibration method

In this section the physical correction process is described. First, the basic concept as well as the new spectral temperature and cosine correction are presented. The basic concept is then used to explain the correction method in the field.

3.1 Basic concept of the physical correction

The basic concept behind the physical correction function is illustrated in Figure 6.

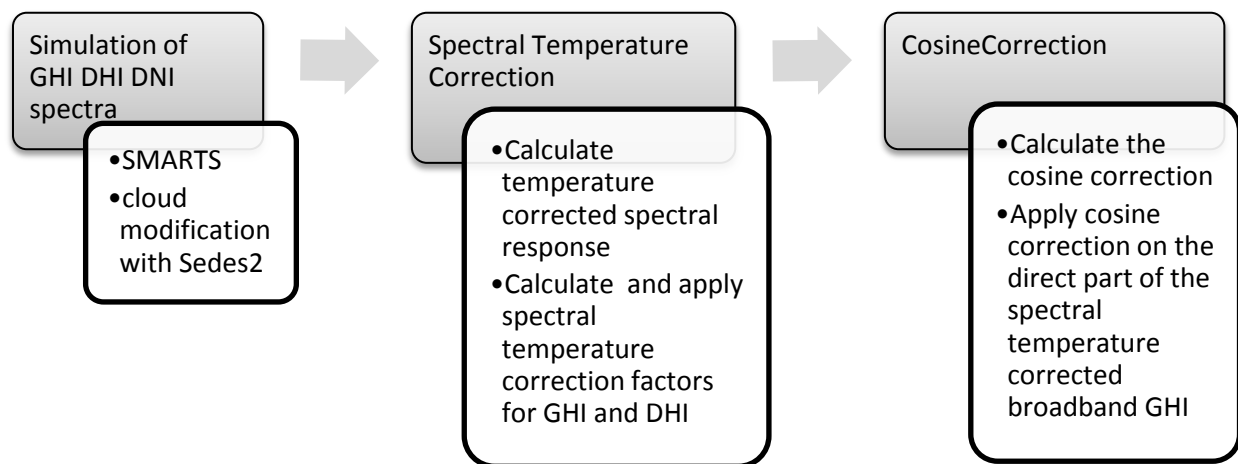


Figure 6: Basic concept of the physical correction

At first, the current DNI, GHI and DHI spectra are simulated with the clear sky radiative transfer model SMARTS 2.9.5 and modified for the presence of clouds using the enhanced Sedes2 model with the best available input parameters. The resulting spectra are then used to calculate the temperature corrected spectral response for the current temperature. With that spectral response and the current spectrum, a combined spectral and temperature correction factor can be calculated for GHI and DHI, respectively.

This combined spectral and temperature correction factor compensates the spectral error for the apparent spectrum and the specific spectral response of the photodiode sensor. Then, a cosine correction is calculated and applied to the direct part of the spectral temperature corrected broadband GHI. The result is a spectral temperature and cosine corrected GHI, a spectral temperature corrected DHI and the associated DNI. One main goal of the physical correction method is the reduction of the location dependence of the set of calibration factors and measurement corrections.

In the following, the involved determination of the specific spectral response and following spectral temperature correction as well as the involved cosine correction are described in detail.

3.1.1 Simulation of the GHI, DHI and DNI spectra

The simulation of the spectrum is carried out with a combination of SMARTS 2.9.5 and an enhanced version of the Sedes2 code as explained in section 2.1. The required input, which is also described in section 2.1, for these calculations is obtained as follows.

The ambient temperature, relative humidity and pressure are measured at a reference meteorology station. With the information about the location of the sensor and the current time stamp, it is possible to calculate the current true sun height and the apparent solar height angle with refraction along equations by (Michalsky, 1988). With the calculated sun position it is then possible to calculate the pressure corrected, uncorrected and altitude corrected air mass as done by (Kasten & Young, 1989). The current CO₂ concentration is estimated with a simple model including the seasonal variation of CO₂ provided by Olsen (Olsen & Randerson, 2004) along the method described by [(Wilbert, 2014), p.56]. The, possibly season dependent, surroundings of the sensor have to be evaluated by the user and corresponding albedo settings must be selected. A number of pre-set surroundings are already implemented in SMARTS 2.9.5 (Gueymard, 2005).

Some of the input parameters are obtained from different sources depending on whether or not the corrections are performed during the calibration of the RSI or during its application in the field. During the calibration some input parameters are obtained by reference sensors such as an Aeronet station, which are typically not available for a RSI based measurement campaign.

During the calibration, aerosol data from a nearby Aeronet station can be used to calculate the Angstrom exponents α_1 , α_2 and the Angstrom turbidity coefficient β as described by (Wilbert, 2014). They are related to the AOD by Eq. (3). The needed broadband single scattering albedo and asymmetry factor are being calculated by weighing their spectral components with a GHI spectrum under G173 atmospheric conditions at a rough estimate of the apparent air mass (ASTM, 2012; Wilbert, 2014). The Angstrom exponents, single scattering albedo and asymmetry factors describe the currently present aerosol type (cf. section 2.1). The Aeronet station also provides an accurate measurement of the apparent ozone concentration in [Dobson] and the apparent precipitable water vapor in [cm]. All these parameters have to be estimated for the application of the RSI in the field. This will be described in section 3.3.

Using these values, the spectrum can be estimated with a SMARTS 2.9.5 simulation. The resulting spectra for GHI and DNI are then corrected with the Sedes2 cloud modifier. For this correction, the most

accurate available measurements of the broadband GHI and DNI are used to determine the right cloud modifier. During the calibration these values come from the reference station, which is located directly next to the RSI under calibration and which uses thermopile radiometers. For the application of the method at a remote site without a reference station the best available preliminary GHI and DNI from the RSI are used as further explained section 3.3. The cloud corrected spectra for GHI and DNI are then used to calculate the DHI cloud corrected spectrum with the apparent solar zenith angle along the transformed Eq. (1):

$$DHI = GHI - DNI \cdot \cos SZA. \quad (15)$$

This equation applies to broadband irradiances as well as for each wavelength as explained in section 2.1.

All of the steps described above lead to the estimation of the apparent GHI, DHI and DNI spectrum that is received by the photodiode-based pyranometer, mounted in the RSI.

3.1.2 Description of the combined spectral and temperature correction

As previously explained in section 2.3, the used c-Si pyranometer in the RSI has a temperature dependent spectral response. The temperature effect is especially dominant around 1073nm. Additionally, the spectral response is not uniform for all wavelengths of the incoming irradiance. Therefore, the responsivity (cf. Eq. (8)), which is the output signal of the silicon pyranometer and depends on the spectral response, is dependent on the current spectrum and the temperature.

In order to incorporate the temperature dependence of the spectral response into the spectral correction, the wavelength per temperature shift of the quantum efficiency described by (Hishikawa et al., 2018) for silicon based photovoltaic devices is used (as previously referenced in section 2.3).

Essentially, Hishikawa proposes that with a known spectral response at one temperature T_1 , the quantum efficiency at that temperature can be calculated with Eq. (8) in section 2.3. The wavelength, at which the quantum efficiency is maximum λ_{max} , is then determined.

To calculate the quantum efficiency at a desired temperature T_2 , the quantum efficiency at temperature T_1 is shifted by $-0.45\Delta T \frac{nm}{K}$ in wavelength above λ_{max} . ΔT is the temperature difference between T_1 and T_2 . Below λ_{max} the quantum efficiency at T_2 equals the quantum efficiency at T_1 (Hishikawa et al., 2018):

$$QE(\lambda, T = T_2) = \begin{cases} QE\left(\lambda - 0.45 \frac{nm}{K} \cdot \Delta T, T = T_1\right), & \lambda > \lambda_{max} \\ QE(\lambda, T = T_1) & , \lambda \leq \lambda_{max} \end{cases} \quad (16)$$

Finally, the quantum efficiency at T_2 is converted back to the spectral response at T_2 with Eq. (8) in section 2.3.

The manufacturer of the silicon pyranometer provides a generic spectral response (Licor, 2004). It is not clear from the provided information by (Licor, 2004) at which temperature this spectral response is

measured. This thesis assumes the temperature as $T_{ref} = 25^\circ\text{C}$ because this is the standard temperature for laboratory conditions.

Using the above described method with the generic spectral response, the spectral response at different temperatures can be calculated. The calculated spectral responses at two temperatures as well as the spectral response at reference temperature are displayed in Figure 7.

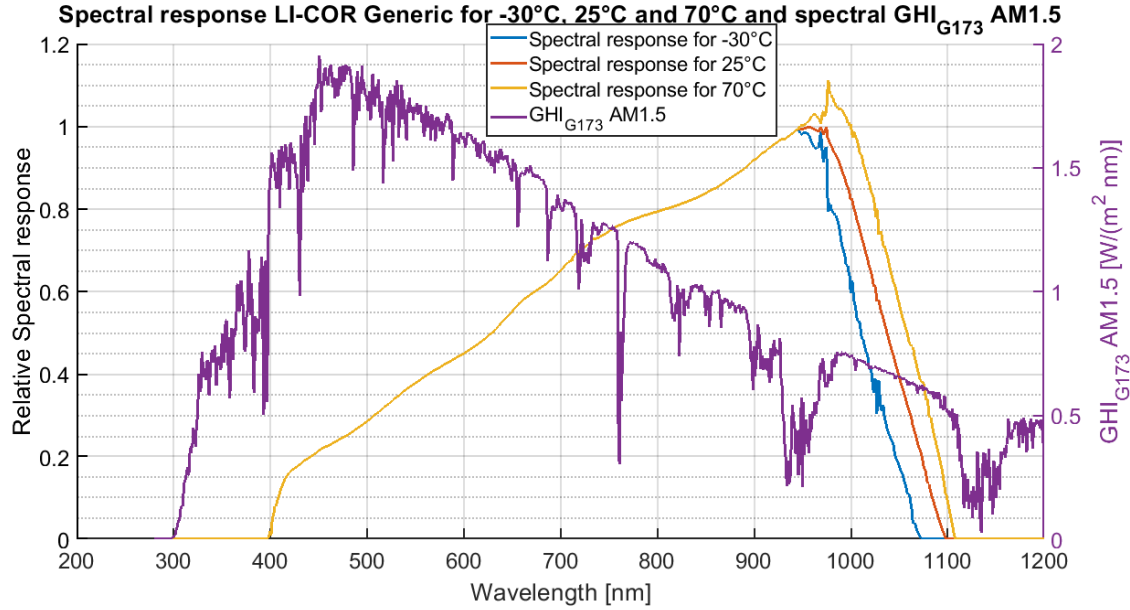


Figure 7: Calculated spectral response of the LI-200 at -30°C , 25°C and 70°C and the GHI under G173 air mass 1.5 atmospheric conditions (ASTM, 2012). The spectral response for 25°C is from (Licor, 2004) and is assumed to be 25°C as a standard laboratory temperature.

Figure 7 shows the obtained spectral response curves for different temperatures for -30°C , 25°C and 70°C as calculated with the model and the GHI spectrum under G173 atmospheric conditions at an air mass of 1.5 for comparison (ASTM, 2012). As discussed in section 2.3, the temperature effect on the spectral response is especially dominant around 1073nm, the indirect band gap of silicon. This illustrates that the spectral temperature dependence of the spectral response is not negligible, especially in hot climates.

After calculating the spectral response at the current sensor temperature, the responsivities can be calculated, using Eq. (8). The integrals are carried out numerically using trapezoid integration as defined in (ASTM, 2016). With the obtained average responsivities, the spectral temperature correction factor $F_{\alpha F}$ can be defined:

$$F_{\alpha F} = \frac{\int d\lambda SR(\lambda, T_{ref}) \cdot Spectrum_{G173}}{\int d\lambda SR(\lambda, T_{curr}) \cdot Spectrum_{curr}} \cdot \frac{\int d\lambda Spectrum_{curr}}{\int d\lambda Spectrum_{G173}} = \frac{R_{ave}^{ref}}{R_{ave}^{curr}} \quad (17)$$

Where T_{ref} is the reference temperature, here 25°C , T_{curr} the current temperature, $Spectrum_{G173}$ the reference spectrum under (ASTM, 2012) standard conditions for $AM = 1.5$ and $Spectrum_{curr}$ the current spectrum of the incoming irradiance.

This spectral temperature correction factor $F_{\alpha F}$ has the advantage that it corrects the measurement of the RSI to standard conditions (G173 spectra for air mass 1.5 (ASTM, 2012) and $T_{ref} = 25^\circ C$), which is useful for the later definition of calibration factors (see section 3.2 below). It also combines the temperature and spectral correction into one correction factor.

With the previously estimated spectra (cf. 3.1.1 above) the spectral temperature correction factors $F_{\alpha F}$ for the GHI and DHI spectra and the current sensor temperature can be calculated and applied. This results in spectral and temperature corrected GHI and DHI measurements.

As briefly explained in section 2.3, each LI-COR 200 sensor is calibrated beforehand by LI-COR Biosciences under “natural daylight conditions” [(Licor, 2004), p.7]. The obtained calibration factor, commonly referred to as LI-COR constant, is known for each used sensor and applied to the measurements of the GHI, DHI and DNI by default through the data logger program (Jessen et al., 2017). Using this calibration method, the LI-COR constant is a GHI calibration factor and can not necessarily be applied to the DHI measurement because of the different spectra of GHI and DHI.

Therefore, the LI-COR constant has to be transformed onto the spectrum of the DHI before applying it. This is achieved by calculating $F_{\alpha F}$ with the LI-200 spectral response (Licor, 2004) and the GHI spectrum under G173 air mass 1.5 atmospheric conditions (ASTM, 2012) as reference spectrum and DHI spectrum under G173 air mass 1.5 atmospheric conditions (ASTM, 2012) as current spectrum (cf. Eq. (17)). This factor is 1.2787 and is applied to the DHI measurement of the RSI additionally to the LI-COR constant, before the measurements are corrected further. The G173 atmospheric conditions are used as a coarse reference because the actual spectrum under which the sensor was calibrated is unknown (Licor, 2004).

Comparison of the thus obtained temperature correction to pre-existing temperature corrections

(King & Myers, 1997) and (Geuder et al., 2008) calculated a broadband temperature correction F_α (cf. section 2.31) that can now be compared with $F_{\alpha F}$. The slope of the broadband temperature correction obtained by (King & Myers, 1997) is $\alpha_K = -0.00082$ 1/K and the slope obtained by (Geuder et al., 2008) is $\alpha_G = -0.0007$ 1/K. Figure 8 shows the temperature correction factors as a function of the sensor temperature. The curve $F_{\alpha K}$ is the temperature correction function (cf. Eq. (10)) calculated with α_K and $F_{\alpha G}$ is calculated with α_G .

To compare the new correction to these functions from the literature, $F_{\alpha F}$ is calculated for a fixed GHI spectrum under G173 atmospheric conditions at a specific air mass and different temperatures. When $F_{\alpha F}$ is then plotted against the temperature (cf. Figure 8), one obtains the slope α as defined by (King & Myers, 1997) and (Geuder et al., 2008). An $\alpha = -0.000834$ 1/K for an air mass of 4 and an $\alpha = -0.000786$ 1/K for an air mass of 1 is obtained (Vignola et al., 2018). $F_{\alpha F}$ is shown in Figure 8 for the different slopes.

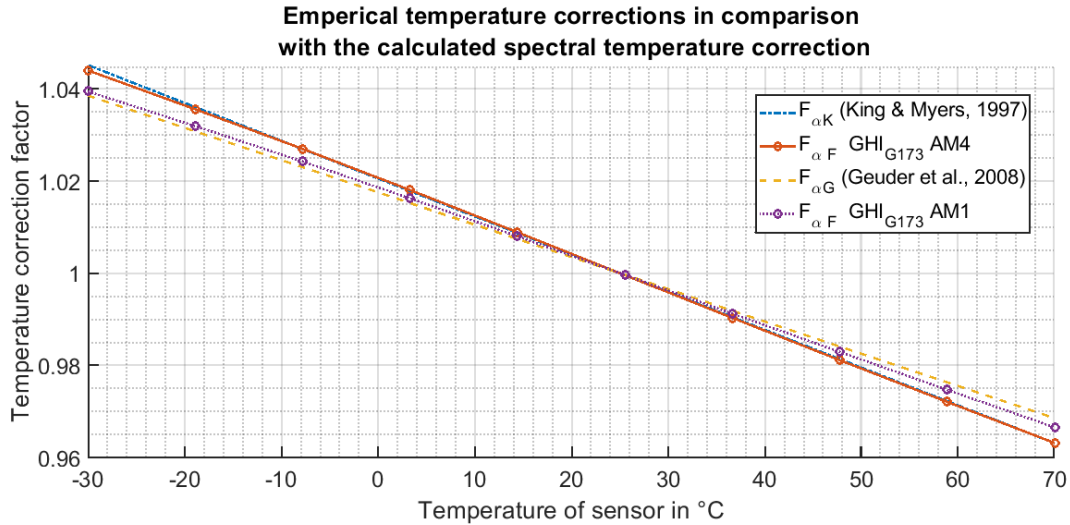


Figure 8: Spectral temperature correction factor $F_{\alpha F}$ in comparison with currently used broadband temperature correction factors.

The measurements carried out by (Geuder et al., 2008) to obtain $F_{\alpha G}$ were conducted at the PSA, Spain. For the experiment, the used LI-COR200 was cooled down to 0°C and then mounted outside close to solar noon. As the sensor heated up to 40°C, the sensor signal was measured as well as the temperature inside the sensor. To account for possible changes of the irradiance during the measurement campaign, a reference photodiode at a constant temperature measured the irradiance close by (Geuder et al., 2008).

A review of the original data set of (Geuder, 2008) and the facts that the experiment was conducted around solar noon and with a high maximum temperature lead to the conclusion that the experiment was conducted in midsummer. The high SZA around solar noon in midsummer leads to the assumption that the air mass at the time of the experiment was not much above one. As Figure 8 shows, the newly obtained $F_{\alpha F}$ for air mass 1 ($F_{\alpha F}$ GHI_{G173} AM1) fits the curve obtained by (Geuder et al., 2008), $F_{\alpha G}$, quite well especially in the region of the conducted experiment from 0°C to 40°C.

It could not be determined exactly under which specific spectral conditions the experiment from (King & Myers, 1997) was conducted. The publication states that the temperature correction was determined with a routinely used standard for photovoltaic cells (King & Myers, 1997). The used standard has been updated since the publication by (King & Myers, 1997) so that the exact procedure could not be determined. The resulting $F_{\alpha K}$ from (King & Myers, 1997) can be reproduced using AM 4.

3.1.3 Description of the new cosine correction

As discussed in section 2.3, the sensors response changes with different AOIs. The data sheet of the used LI-200 sensor states, that the diffusor head is cosine corrected up to 80° AOI (Licor, 2004). This is not sufficient because the sensor is also operated in early mornings and late evenings where the AOI is between 80° and 90°.

For this reason, a cosine correction is developed from two measurement series, where two sensors are illuminated with a small light source in a darkened room under different AOI^A. The different AOIs are achieved by rotating the LI-200 sensor as well as a reference sensor with respect to the light source. The reference sensor measures the change in intensity of the lamp. The final measurements of the LI-200 are corrected for the intensity change of the lamp and are conducted with accuracy to the fifth significant digit for the sensor's output signal. The then obtained correction factor F_{cos} corrects the signal to the ideal cosine of the current AOI. Because of the measurement technique, the correction factor can be applied as a stand-alone function to the DNI as opposed to the currently published cosine and cat ear correction factors that depend on the air mass correction function and are applied to the GHI (cf. section 2.3.1) (Geuder et al., 2008; Augustyn et al., 2004; King & Myers, 1997; Vignola, 2006). Between 0° and 80° AOI, the correction factor varies between 1 and 0.96 and above 80° AOI between 0.94 and 1.4.

This cosine correction factor is applied to the direct component of the spectrally and temperature corrected GHI along the following formula:

$$GHI_{spec\ temp\ cos} = (GHI_{spec\ temp} - DHI_{spec\ temp}) \cdot F_{cos}(SZA) + DHI_{spec\ temp} \quad (18)$$

To obtain the final RSI measurements, the calibration factors are applied. Since the spectral correction is different for DHI and GHI, two calibration factors g and d are defined for GHI and DHI respectively. The fully corrected GHI and DHI measurements of the RSI are calculated as follows:

$$GHI_{final} = g \cdot GHI_{spec\ temp\ cos} \quad (19)$$

$$DHI_{final} = d \cdot DHI_{spec\ temp} \quad (20)$$

From the final resulting GHI_{final} and DHI_{final} , the corresponding DNI_{final} can be calculated along Eq. (1). The calibration method and application of the corrections and calibration factors in the field are described in the following two sections 3.2 and 3.3.

3.2 Calibration procedure

Because of the simulation of the spectra during the physical correction, additional reference sensors are needed for the calibration of the RSIs. First of all, just like for (Geuder et al., 2008) and (Vignola, 2006), a reference station with a tracked pyrhelimeter measuring the DNI and two thermopile pyranometers, one equipped with a tracked shadow ball is needed (cf. section 2.2). From this station comes the input for the reference GHI, DHI and DNI. A meteorology station is needed to measure the pressure, ambient temperature and relative humidity. Additionally, an Aeronet station should be present in the near field of the measuring campaign and provide the ozone concentration, precipitable water vapor and measurements for the calculation of the Angstroem turbidity factor and exponents, single scattering albedo and asymmetry factor throughout the entire calibration campaign. The RSI itself needs to have an internal temperature sensor to measure the temperature of the photodiode sensor.

^A The used data set is conducted by A. Driesse, PV Performance Labs Germany and is confidential. It can therefore not be shown in this thesis.

After the measurements are conducted, the raw data is screened and filtered in order to calibrate only with trustworthy measurement data. To calibrate the RSI, its measurements are corrected using the basic concept of the physical correction (cf. section 3.1 and Figure 6). A detailed flowchart of all steps of the calibration method is given in Appendix I on page 50. In summary, the spectra of the GHI and DHI are simulated for each time stamp with SMARTS 2.9.5 and cloud modified with Sedes2. Using the apparent temperature of the silicon pyranometer, the spectral response is calculated for each time stamp as well. Then, the spectral and temperature correction factor $F_{\alpha F}$ is calculated for each time stamp using the specific spectrum and spectral response. Because the spectra of the GHI and DHI are fundamentally different, $F_{\alpha F}$ is calculated separately for both irradiance components.

Up until here, everything, except for the spectral response, which is calculated with the internal temperature sensor of the RSI, is calculated with measurements from reference sensors. Now, the raw GHI and DHI are multiplied with the LI-COR constant. The DHI is additionally multiplied with the transformation factor of 1.2787 described in section 3.1.2. Each obtained GHI measurement value is then multiplied with the appropriate $F_{\alpha F}^{GHI}$ and each obtained DHI measurement value is multiplied with the correspondent $F_{\alpha F}^{DHI}$ resulting in $GHI_{spec\ temp}$ and $DHI_{spec\ temp}$. Because of the cosine dependence of the direct part of the GHI, each individual $GHI_{spec\ temp}$ is cosine corrected along Eq. (18). The $GHI_{spec\ temp\ cos}$ and $DHI_{spec\ temp}$ are now physically corrected.

To obtain a calibration factor for the GHI, the RMSD of the difference between the $GHI_{spec\ temp\ cos}$ times a variable calibration factor and the reference GHI over the entire calibration time is minimized. The thus resulting calibration factor g is then applied to the $GHI_{spec\ temp\ cos}$ along Eq. (19), resulting in GHI_{final} . In order to calculate the calibration factor for the DHI, the RMSD is minimized with respect to the absolute deviation between the calculated DNI, from the GHI_{final} and the $DHI_{spec\ temp}$ times a variable calibration factor, and the reference DNI, leading to the calibration factor d . DHI_{final} is then obtained with Eq. (20).

The results are the final corrected measurements GHI_{final} , DHI_{final} and the DNI_{final} , which is calculated from the final GHI and DHI along Eq. (1) and the calibration factors g and d . These calibration factors are referenced to standard conditions (G173 AM of 1.5 (ASTM, 2012) and 25°C sensor temperature) and can therefore be applied in the field if the measurements are corrected to these standard conditions as well. That way, the location dependence of the calibration is reduced.

3.3 Estimation of the spectra for the application of the correction method

As mentioned above in section 3.1 some, of the input parameters used for the estimation of the spectra during the calibration are not available for most RSI measurement campaigns. These parameters are those measured with the nearby Aeronet station and of course the reference irradiances. Especially the aerosol parameters (α_1 , α_2 , single scattering albedo and asymmetry factor) and AOD are of importance and complex to determine. The process will be outlaid in the following for an already measured time range from the RSI. In Appendix II a flowchart of the entire correction method can be found.

First, just like during the calibration, the solar position, different air masses and average temperature are calculated. Additionally, the precipitable water vapor is calculated along the formula provided by

(Gueymard, 1993) (cf. Eq. (4)). Aerosol parameters, such as the Angstrom exponents α_1, α_2 , the single scattering albedo and the asymmetry factor are set to temporally constant values. They are derived by evaluating a year of Aeronet data from the station that is expected as most representative for the site of interest and defined beforehand. The spectral single scattering albedo and the asymmetry factors are calculated from the Aeronet data sets as described by (Wilbert, 2014) are averages over time. These temporal averages are then spectrally weighted with the GHI spectrum under G173 air mass 1.5 spectral conditions (ASTM, 2012) to obtain the broadband single scattering albedo and asymmetry factor required for SMARTS 2.9.5. It is possible to provide seasonal values for these four parameters if more detailed information is available. In this thesis, a year of reference ozone concentrations is provided by the reference Aeronet station to the correction method to account for the large seasonal dependence of the ozone concentration over the course of one year. This is done as a test and can be improved in the future. Instead of Aeronet data also other data sources could be used, i.e. satellite derived information, for the estimation of the ozone concentration.

Now, the current AOD has to be estimated in order to simulate the spectrum appropriately. The AOD at 550nm can be calculated with the Linke-Ineichen turbidity (cf. Eq. (7)). The input parameters for the calculation of the Linke-Ineichen turbidity include the current DNI (cf. Eq. (5) and (6)). It is important that this DNI is not affected by any clouds in front of the sun [(WMO, 2014), p. 183]. If the AOD is calculated for these timestamps it is estimated too high because absorption effects from the cloud and the present aerosols are mixed. It is therefore crucial to identify the sunny timestamps, i.e. no cloud is masking the sun, and only estimate the AOD at 550nm for these time stamps from the Linke-Ineichen turbidity. For the calculation of T_L it is less important if clouds are present somewhere else in the sky.

For the calculation of the Linke-Ineichen turbidity, only the measured DNI from the RSI is available. This DNI is not yet corrected because an estimation of the spectrum is needed for the spectral temperature correction. But a simulation of the spectrum can only be done with a good estimation of the AOD for which T_L is needed. In order to solve this problem, an iteration process is started, which is described in the following and shown in Figure 9.

Preliminary to the cloud detection and the iteration process, a spectral temperature correction is done with the most basic assumptions about the spectrum. This is necessary, in order to detect clouds and start the iteration process from a better initial estimation. This preliminary correction is done with an estimation of the GHI, DHI and DNI spectra using an air mass of 1.5 and a default turbidity. With the obtained spectra, a spectral temperature correction and cosine correction is performed on the entire GHI and DHI time series, which are already multiplied with the calibration factors g and d . These corrections result in the preliminary measurements GHI_{prelim} and DHI_{prelim} from which DNI_{prelim} is calculated using Eq. (1).

In order to identify the sunny time stamps, a cloud checker is used. It first calculates T_L with DNI_{prelim} for each time stamp and then analyzes its temporal gradient. A cloud is detected if an upper threshold of 13 for the Linke-Ineichen turbidity is exceeded or if T_L varies strongly over time, i.e. a difference of more than 0.6 between two time stamps that are apart by 30 min. The DNI is then compared to the clear sky DNI, which is derived from the lowest T_L in the examined time series. If one examined time

stamp is $x\%$ lower than the clear sky DNI, the time stamp is interpreted as cloudy. x is a variable threshold that depends on the air mass. Time stamps at solar noon with deviation larger than 10% are classified as cloudy, however, time stamps at sun rise have to reach a deviation of 30% (Meteorology Group, August 2018).

For the thus obtained sunny time stamps, the iteration process, displayed in Figure 9, is started with GHI_{prelim} , DHI_{prelim} and DNI_{prelim} . First, the Linke-Ineichen turbidity is calculated along Eq. (5) and (6) using DNI_{prelim} . Then, the AOD at 550nm is calculated using Eq. (7) and the obtained T_L . With this AOD at 550nm and all other input parameters (see above), the spectra of GHI, DHI and DNI are simulated with SMARTS 2.9.5 and cloud corrected with Sedes2. The cloud modification is necessary because clouds can still be present in the sky and affect the spectra. With the modified spectra of the GHI and DHI, the specific spectral temperature correction factor for GHI and DHI, $F_{\alpha F}^{GHI/DHI}$, is calculated along Eq. (17) (c.f. section 3.1.2). The GHI and DHI, already multiplied with their respective calibration factors, are then spectral temperature corrected and the GHI additionally cosine corrected as described in section 3.1.3.

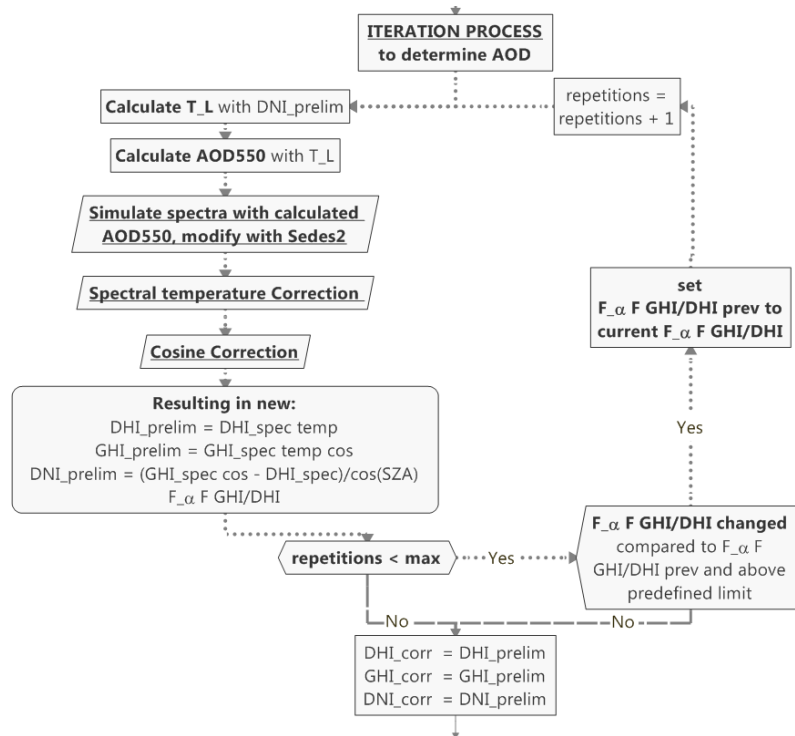


Figure 9: Iteration process of the correction method for the most accurate estimation of the AOD with the available DNI measurement of the RSJ.

This results in $DHI_{spec temp}$ and $GHI_{spec temp cos}$, which define a new set of preliminary measurements for the examined sunny time stamp. From these two preliminary results, a new DNI_{prelim} is calculated using Eq. (1).

Now, the break conditions of the iteration process are examined. If the spectral temperature correction factors $F_{\alpha F}$ for GHI and DHI deviate more than 0.0005 from the previous correction factors and are above a predefined limit of 1.1, the iteration is repeated until a maximum of 10 repetitions is reached. If any break conditions are met, the next sunny time stamp is processed until AOD550 estimations for all sunny time stamps exist.

Finally, all time stamps where the sun is masked can be physically corrected using the temporally closest estimated AOD550 as an input parameter. With this input, the physical correction is made following the basic principle described in section 3.1 and Figure 6. This results in the spectral temperature cosine corrected GHI, the spectral temperature corrected DHI and the corresponding DNI as final corrected measurements. It should be emphasized that the only difference between the calibration method and the correction method is the estimation of the AOD because of the lack of reference sun photometers in the field.

3.4 Summary

A new physical correction method has been developed for Rotating Shadowband Irradiometers. The correction is based on the change of the spectral response with the temperature as well as the difference in responsivity for different incoming spectra. It was shown, that the spectral temperature correction could reproduce the different broadband temperature corrections from (King & Myers, 1997) and (Geuder et al., 2008) by varying the input spectrum. A new cosine correction is developed as well that can be applied directly on direct contribution of the GHI.

In summary, a physical correction contains three steps:

1. The estimation of the spectrum with SMARTS 2.9.5. and the enhanced Sedes2 using the best available input parameters either from reference stations in the calibration process or from the iteration process during the correction in the field
2. The spectral and temperature correction, which references the average responsivity with the spectral response at the current sensor temperature and the estimated current spectrum to standard conditions (G173 atmospheric conditions at air mass 1.5 (ASTM, 2012) and 25°C).
3. The cosine correction on the direct part of the GHI.

The GHI calibration factor g is obtained through RMSD minimization of the corrected GHI with respect to the reference GHI. Through RMSD minimization of the corrected DHI with respect to reference DNI, the DHI calibration factor d is calculated. They are both referenced to standard conditions.

4 Experimental setup and evaluation of the method performance

Within this section the experimental set-up inclusive the used sensors of calibration stations and field measurements is explained. The results of the correction and calibration methods at different locations are shown and then discussed. Finally, an analysis of the improvement of the method is conducted.

4.1 Motivation

In order to quantify the correction results, two sensors are calibrated at one location. They are then deployed at two different locations in different climates than the calibration station. The measurements are then corrected with the newly developed correction method, the correction by (Geuder et al., 2008) and the correction by (Augustyn et al., 2004; King & Myers, 1997; Vignola, 2006).

4.2 Measurement sites, used sensors and datasets

In this thesis, the following three locations are considered to test the new calibration and correction function and to compare them to the pre-existing set of calibration and correction functions by (Geuder et al., 2008) (referred to in the following as Geu) and (Vignola, 2006) (referred to in the following as Vig).

The Plataforma Solar de Almería (PSA) (37.091°N 2.358°W) in Tabernas, Spain at an altitude of 500m above mean sea level is located in an arid, steppe, cold arid climate (BSk) (DLR, 2018; Kottek, 2005). The reference station at the PSA is equipped with a Kipp&Zonen pyr heliometer (model CHP1), mounted on an automated tracker and Kipp&Zonen thermopile pyranometers for the measurement of the GHI and the DHI (model CMP21) (DLR, 2018). An Aeronet station near to of the reference and calibration station provides level 2.0 data, which is fully cloud filtered and calibrated, on atmospheric parameters for most of that time range (Aeronet, August 2018d). For one of the examined sensors (RSI-PY87333-1) one year of reference and RSI data from January 2015 to February 2016 are available from this site. This sensor was then deployed at NETRA, India (cf. below). For the other examined sensor (RSI-PY88668-1), four months of reference and RSI data from April to August 2016 are available. But the Aeronet station was only online from June to August 2016, which is why the calibration data set is reduced to that time range. This sensor was then deployed in Londrina, Brazil (cf. below).

The NETRA station is deployed in Greater Noida, New Delhi, India (28.5019°N 77.465°E) at an altitude of 195m above mean sea level in a warm temperature, winter dry, hot summer (Cwa) climate (DLR, 2018; Kottek, 2005). Reference and RSI data from June 2016 to August 2017 are available. The reference station at NETRA is also equipped with a Kipp&Zonen pyr heliometer (model CHP1), mounted on an automated tracker and Kipp&Zonen pyranometers (model CMP21) for the measurement of the GHI and DHI (DLR, 2018). The nearest Aeronet station, that measured in the desired time range, is located in Gual Pahari (28.4258°N 77.150°E) at an altitude of 250m above average sea level, which is about 32km away from the station (see also the map in Appendix III on page 53) and provides 1.5 level Aeronet data (Aeronet, August 2018b; Google Earth, 2018). For the estimation of the Angstroem parameters, symmetry and asymmetry factor, level 2.0 Aeronet data from 2009 from the site in New Delhi (28.630°N 77.175°E) at an altitude of 240m above sea level is used (Aeronet, August 2018c). This choice is made because this station is located in the main wind direction from NETRA (see also the map in Appendix III on page 53). That way, a better estimation of the aerosol type at NETRA can be made.

The Lon station is deployed in Londrina, Paraná, Brazil in a warm temperature, fully humid, warm summer (Cfb) climate (Kottek, 2005). The used reference and RSI data from November 2017 to May 2018 is kindly provided by Fotovoltec Solar Engineering through CSP Services. The reference station at Lon is equipped with a pyr heliometer, mounted on an automated tracker for the measurement of the DNI and pyranometers for the measurement of DHI and GHI. The nearest Aeronet stations are about

469km away and located in Campo Grande, Sonda and Sao Paulo (Google Earth, 2018). Campo Grande, Sonda (20.438°S 54.538°W) at an altitude of 677m above average sea level provides 1.5 level Aeronet data for this evaluation (Aeronet, August 2018a). Even though the climate at the site is equatorial, winter dry (Aw) (Kottek, 2005) the site is still chosen as source of Aeronet data because the population of the cities is about the same (Wikipedia, August 2018a, b), both cities are not near the coast and at about the same altitude at different sites of the Rio Paraná (see also the map in Appendix IV on page 55) (Google Earth, 2018).

The here examined RSIs are Twin RSI, one example is shown in Figure 2, manufactured by CSP Services (CSP Services, August 2018). They use a LI- 200 sensor (Licor, 2004) for the irradiance measurements. For this examination, only data in 10 minute resolution that was measured up until 24 hours after a cleaning event is taken into account. This assures that the sensors are not affected by soiling. In addition, the automatic quality control described by (Geuder et al., 2015) is used to discard suspicious data and only solar zenith angle above 85°, GHI and DHI measurements above 10 W/m² and DNI measurements above 300 W/m² are considered (Jessen et al., 2017). All corrected measurements that deviate more than 25% from the reference measurement are assumed to be erroneous and are not used for the calculation of the calibration factors. It has to be stated that the sensors at the NETRA station were cleaned irregularly, which means the available data set is reduced significantly and the used time stamps might be temporally far apart.

4.3 Evaluation method

In order to quantify the performance of the physical calibration and correction method, the two sensors are calibrated at the PSA and then deployed at Lon or NETRA. At both stations the RSI measurements are corrected with (Geuder et al., 2008) (Geu), (Vignola, 2006) (Vig) and not only the physical correction method (Phys) to allow a benchmark. Evaluations are performed using several time ranges at each site. Then, the absolute bias and the root mean square deviation (RMSD) for GHI, DNI and DHI is calculated and compared as a measure for the performance of the calibration and correction methods.

Secondly, an additional calibration is performed at NETRA and the seasonal dependence of the calibration factors at the PSA and NETRA is analyzed.

4.4 Performance with the calibration factors from the PSA at two locations

4.4.1 Correction results with different correction methods at NETRA, India

The corrections of the data from NETRA are done with the calibration factors from one year of calibration time for the physical correction (Phys), Geuder (Geu) and Vignola (Vig). Figure 10 displays the absolute bias and RMSD of the corrected GHI measurements for six different time ranges over the course of one year. The different time ranges are displayed above each subplot. The x axis references the average GHI, measured with the thermopile pyranometer, for each time range.

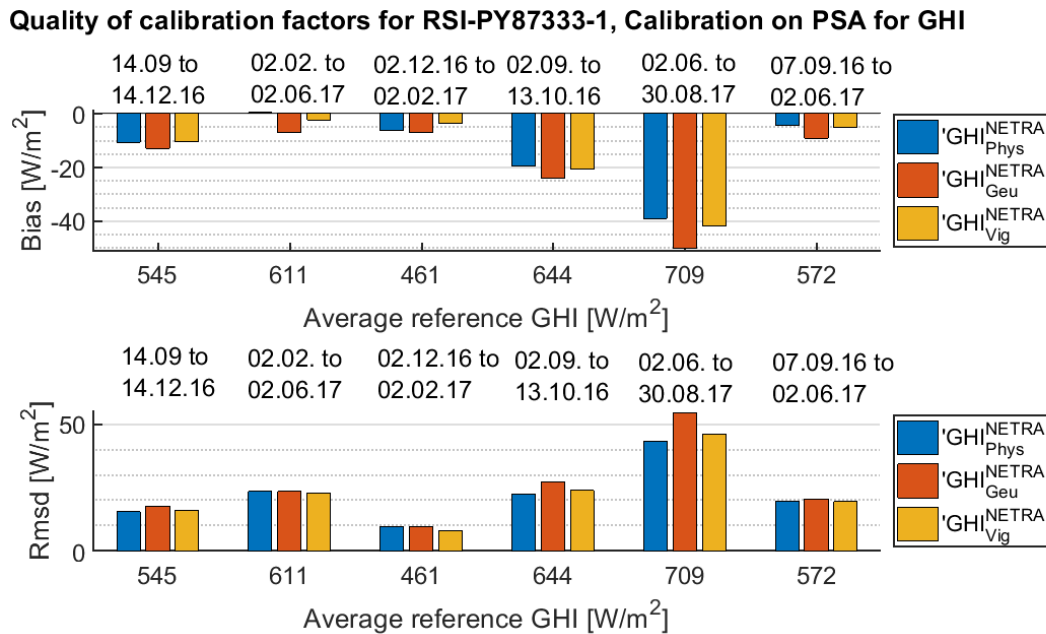


Figure 10: Absolute bias and RMSD of corrected measurements from NETRA with calibration factors from the PSA for the GHI.

The physical correction method is able to reduce the bias of the GHI measurements compared to Geu for all time ranges, compared to Vig a small reduction is found for all but one time range. In two time ranges the application of the physical correction method reduced the RMSD compared to existing methods and otherwise yields nearly the same RMSD for the GHI of the corrected measurements. Compared to Geu, a reduction of the RMSD is found for all time ranges. The RMSD of the physically corrected GHI measurements ranges between 2.1% and 6% relative to the average reference GHI of the evaluated time interval. The highest RMSD occurs in the time range between June 2nd and August 30th, which lies almost completely in the summer monsoon time in New Delhi (Wang & Ho, 2001).

This implies a challenge for the physical calibration method because the last calculated AOD from a sunny time stamp might be days or even weeks old. Especially the high bias in that time range could indicate that the Sedes2 model does not reach a sufficient accuracy for these weather conditions. However, the Phys method still outperformed the other correction methods for this time interval. This indicates that the physical correction method corrects the systematic measurement errors of LI-200 sensor for NETRA better than the pre-existing methods.

Figure 11 displays the bias and RMSD of the corrected measurements after applying the different correction methods for the DNI in the same manner as for the GHI. The reference DNI that is displayed on the horizontal axis is measured with the pyrhelimeter at NETRA for the specific correction time range.

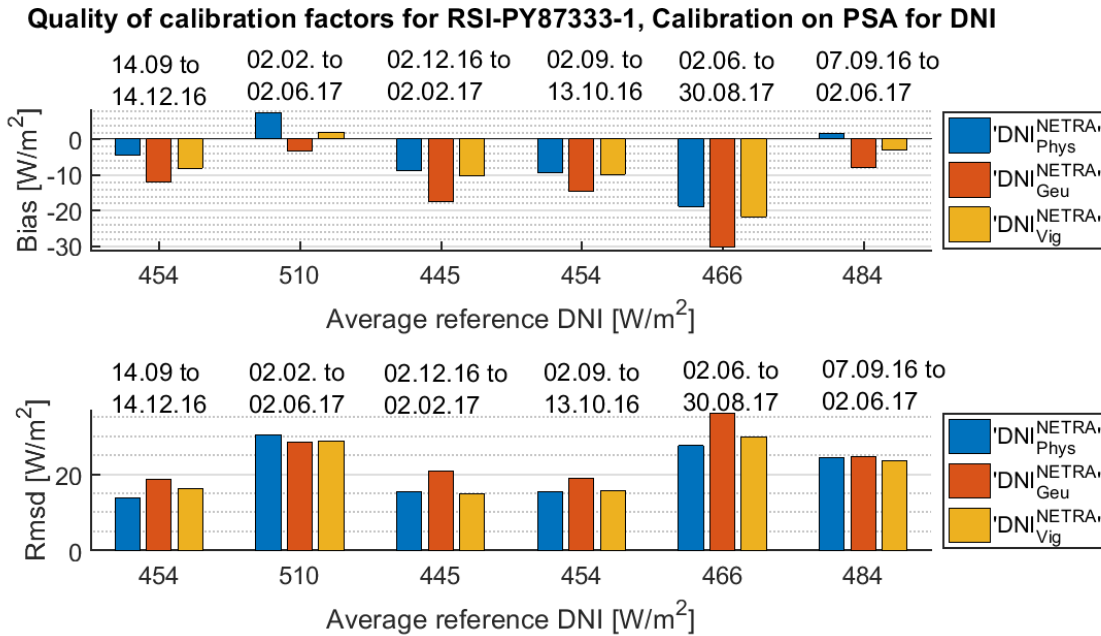


Figure 11: Absolute bias and RMSD of corrected measurements from NETRA with calibration factors from the PSA for the DNI.

Figure 12 shows that the physical correction is able to reduce the bias of the corrected DNI measurements compared to Geu and Vig for all but one time range. This is again remarkable because it shows that the systematic errors of the RSI measurement could be reduced more than with pre-existing methods. The RMSD for the DNI is reduced or equal to the RMSD achieved with Geu for all but one time range and reduced for two time ranges in comparison with Vig. For two time ranges the RMSD is slightly increased in comparison with Vig. One possible explanation could be that the temporally closest AOD at 550nm was not a good representation of the actual present AOD at 550nm and the timestamp was therefore corrected erroneously. Additionally, the Angstrom exponents, which are estimated with Aeronet data from a selected year in New Delhi, might not fit the actually present aerosol type.

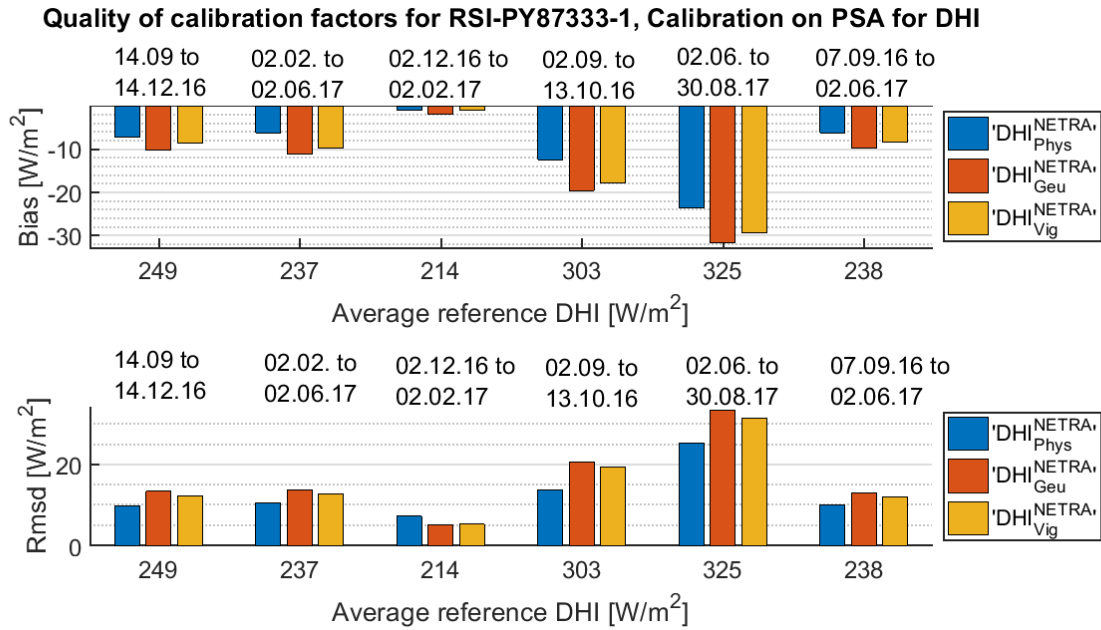


Figure 12: Absolute bias and RMSD of corrected measurements from NETRA with calibration factors from the PSA for the DHI

Figure 12 displays the absolute bias and RMSD for the DHI after the application of the three different correction models in the same manner as for the GHI and DNI. The physical correction method is able to reduce the bias of the measurements for the DHI significantly for all time ranges. (Geuder et al., 2008) and (Vignola, 2006) both make specific DHI corrections to account for measurement errors occurring specifically on days with blue skies. The new correction function is now able to model the current DHI spectrum and can then account for the actually present spectrum of the DHI. The lower bias for all time ranges is a result of this. The RMSD is decreased significantly for all except one time range in comparison with the pre-existing methods. This shows that the physical correction is able to better model the measurement of the DHI by the c-Si LI-COR sensor. In one time range the RMSD is slightly increased in comparison with pre-existing methods, but still only about $7 \frac{W}{m^2}$. Thus, the overall deviation of the DHI is reduced with the new method.

This analysis of the measurement errors shows that the physical correction function is able to reduce the bias of the GHI, DHI and DNI measurements significantly for all time range but one for NETRA. The RMSD is reduced for most of the time ranges for GHI and DNI compared to Geuder and significantly reduced for the DHI component in comparison with Vignola and Geuder. This shows that through the approach based on physical relationships, the physical correction function is able to better model the measurement characteristics of the RSI. A possible reason why the RMSD is not even more reduced for the GHI and DNI might be a wrong estimation of the input parameters describing the aerosols like the AOD and the Angstrom exponents. This is further investigated in section 4.7.2.

However, it is worth pointing out that the good correction results of the physical correction method are achieved already with quite rudimentary estimations of the atmospheric conditions and aerosol type. It

is worth stressing that the estimation of the aerosol properties, α_1 , α_2 , single scattering albedo and asymmetry factor, stem from an evaluation of 2009 in New Delhi, which is about 27km away (Google Earth, 2018) and a major aerosol source. With an improvement of the aerosol input parameters and the Sedes2 model, the measurement errors could be further reduced with the physical correction function (cf. section 4.7.2).

However, the results suggest that the location dependence of the correction with calibration factors from the different climate at the PSA is reduced with the new methods.

4.4.2 Correction results in Londrina, Brazil

The calibration factors from a calibration time of one and a half months, from June 16th to August 30th 2016 at the PSA. The resulting bias for GHI, DHI and DNI of the physically calibrated measurements at the PSA is below 0.5% with respect to the average reference irradiance for each component. The RMSD of the physically calibrated measurements for the GHI is 1.4%, for the DHI 4.1% and for the DNI 1.2% with respect to the respective average reference irradiance in the time range. This shows that the calibration was successful because these quantities matched the biases and RMSD of the calibrated measurements with the pre-existing calibration functions.

The calibration results are tested with the three different correction methods, also used in NETRA (cf. section 4.4.1) at the Lon station in Londrina, Brazil. Five time ranges from Lon are examined, two time ranges of about one month, two of about two months and one ranging the entire available time range of six months. Since the station is located in the southern hemisphere, the time range includes spring, summer and fall at the site. Figure 13, 14 and 15 display the bias and RMSD of the corrected measurements for GHI, DNI and DHI respectively after the different correction methods are applied.

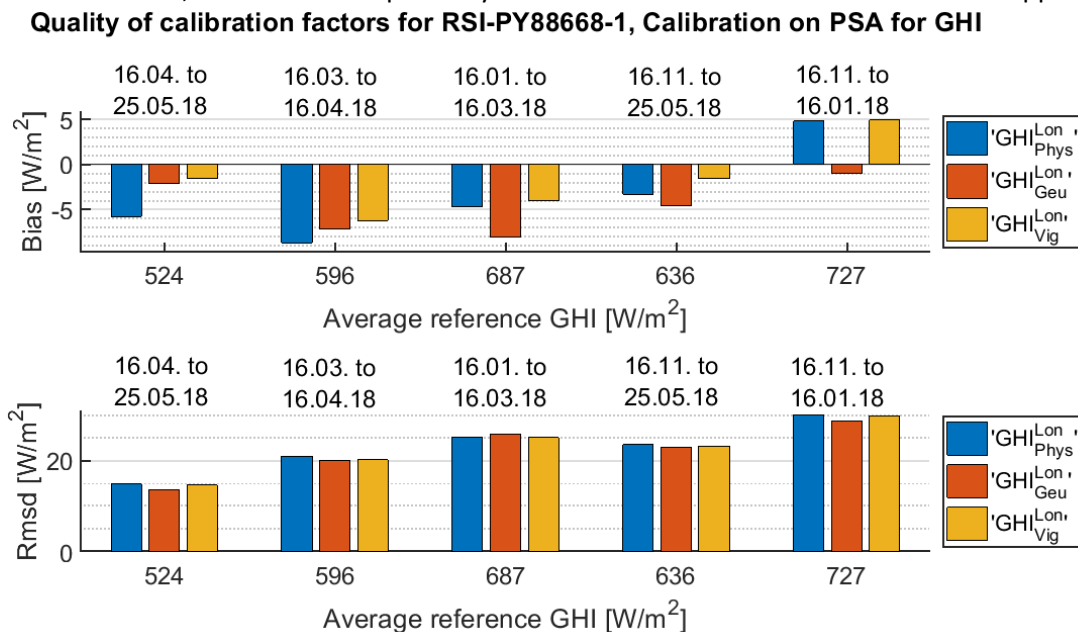


Figure 13: Absolute bias and RMSD of corrected measurements from Londrina with calibration factors from the PSA for the GHI.

The results are shown in the same fashion as the NETRA correction results, with the calibration time range at the top of each subplot and the average reference irradiance from the thermopile sensors from each time interval on the x axis. For three time ranges the bias of the GHI is reduced compared to Geu and for one time range it is decreased in comparison to Vig. For two time ranges the bias for the GHI measurement is increased with the physical method in comparison with the old methods. Overall, the bias of all methods is smaller than 1.5% relative to the reference GHI in that time range. No improvement of the RMSD is achieved with the physical method and the results of all three correction methods are close to each other.

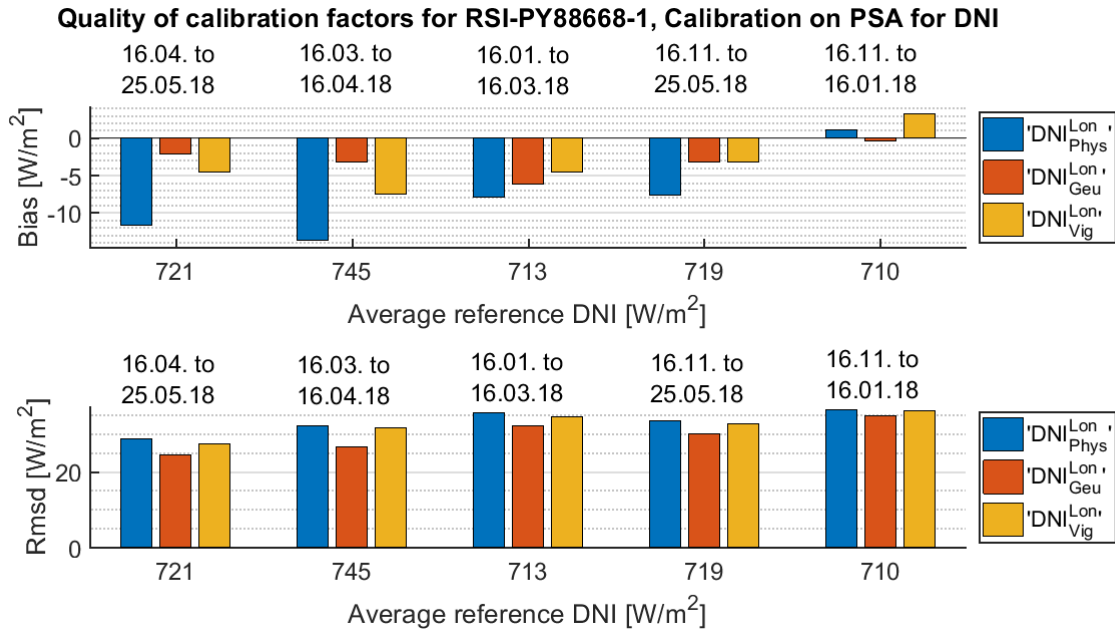


Figure 14: Absolute bias and RMSD of corrected measurements from Londrina with calibration factors from the PSA for the DNI.

For most time ranges, the bias is increased with the new correction method. For the DNI component the RMSD is also slightly increased for all time ranges, but for all calibration methods the RMSD is between ca. 4% and 5%.

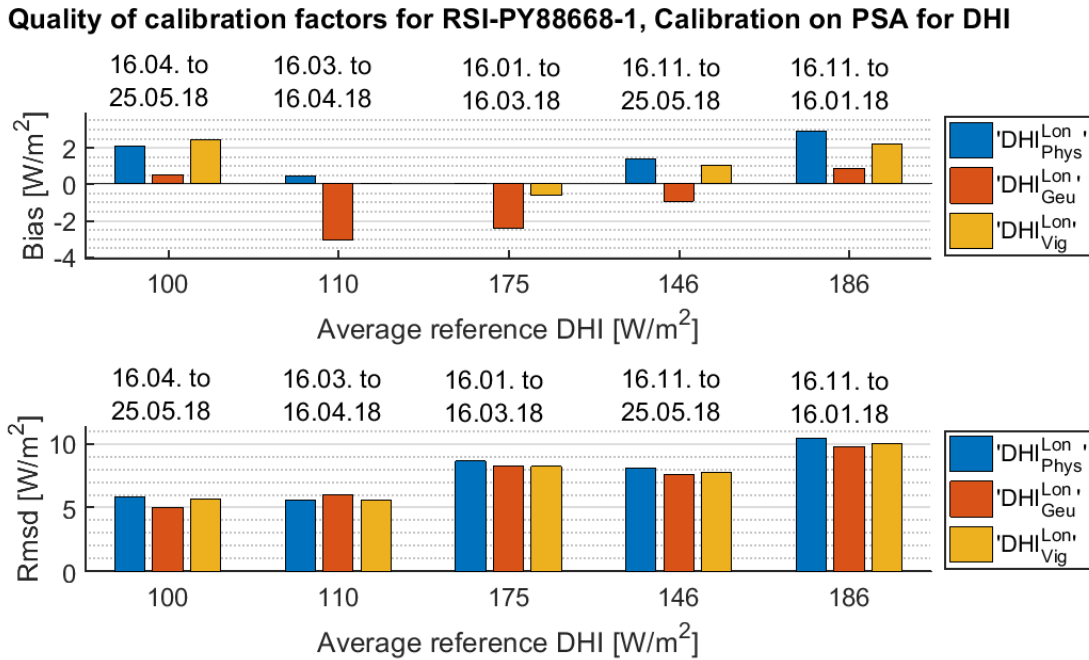


Figure 15: Absolute bias and RMSD of corrected measurements from Londrina with calibration factors from the PSA for the DHI.

The bias of the DHI measurement is reduced for two of five time ranges compared to Vig and reduced for all expect three time ranges compared to Geu with the physical method and does not exceed a bias of roughly 2.5%. The RMSD of the corrected DHI with the physical method is slightly increased for most time ranges, but the RMSD for all correction methods is close together.

There are a few possible explanations for the lack of improvement by the physical correction method. No atmospheric pressure measurement is done in Londrina at the site on ground level. The pressure is therefore estimated with the barometric height formula, which adds an uncertainty to the correction method and could lead to a bias in the correction results. The pressure is used to calculate the precipitable water vapor. The precipitable water vapor and pressure are then used to estimate the AOD at 550nm (cf. Eq. (7)). This is a key factor when simulating the spectrum with SMARTS 2.9.5. If the AOD at 550nm is erroneous the spectrum and therefore the entire physical corrections are erroneous.

An overall improvement of the input parameters especially in regard to the estimation of the Angstroem exponents, single scattering albedo and asymmetry factor should also be done because they stem from an Aeronet station that is about 469km away in a different climate (cf. section 4.2 and also the map in Appendix IV on page 55). Better correction results might even be achieved with estimations of the aerosol type from a station that is further away from Londrina but has a comparable climate and population size.

Another uncertainty factor is the used cloud checker. It is optimized for NETRA, India. In order to distinguish between sunny and masked sun timestamps, the thresholds for clouds are set rather low to account for the high aerosol content (Nouri, July 2018). The application of these thresholds in Londrina

might lead to an erroneous categorization of the timestamps. The corrections could therefore be repeated with an improved version of the cloud checker. In addition, all time ranges that are examined, are heavily impacted by clouds which means that the influence of Sedes2 on the physical correction is quite high even though Sedes2 might not be applicable in Londrina. (Myers, 2012) evaluated simulated spectra and spectral measurements for Miami in Florida and Boulder in Colorado and found high deviations between the computed spectra by Sedes2 and spectral measurements especially in the wavelength range of the here used LI-COR sensor. This shows that the Sedes2 model might not be applicable at every location. It should be investigated if Sedes2 can be adapted to the application at Lon.

The uncertainties concerning the categorization of sunny time stamps could explain the lack of improvement in RMSD for all irradiance components. The possibly wrong input for the aerosol type could explain the increased bias that is observed for the GHI and DNI. Overall, there are many significant uncertainties regarding the results in Londrina due to the quality of the input data. A further investigation should therefore be conducted with the stated optimizations.

4.5 Variability of the calibration factors at the PSA and NETRA

In this section the variability of the calibration factors obtained with the selected calibration interval is analyzed. Five calibrations are conducted at the PSA for different time ranges and different seasons. The obtained calibration factors are then compared to the result from the longest calibration time. Six calibrations are conducted at NETRA and are again compared to the result from the longest calibration time.

At the PSA, five calibration time ranges are examined. Three are two months long, one is one month and another one is one year long. The shorter time ranges are distributed between spring and fall. Figure 16 displays the calibration factors, obtained the Geu, Vig und Phys, for the different time ranges. The respective calibration factors from the longest calibration time are shown as “Cert”^B in the legend. The relative deviation of each calibration factor with respect to the Cert is also displayed in the lower subplot. The calibration time ranges are shown at the top of the first subplot. On the x axis the number of GHI time stamps “NumGHI” and the number of DNI time stamps “NumDNI” are shown. NumGHI references the number measurement points that were used to compute the GHI calibration factors for each calibration method. The GHI calibration factors are labeled with g in the legend. NumDNI is the number of measurement points that were used to calculate the DHI calibration factors, which are labeled d in the legend of the plots. In the case of the Vig calibration, NumDNI is also the number of measurement points that were used to calculate the DNI calibration factor, which is labeled with n in the legend.

^B These calibration factors are in practice then given to the client with a calibration certificate, hence the name.

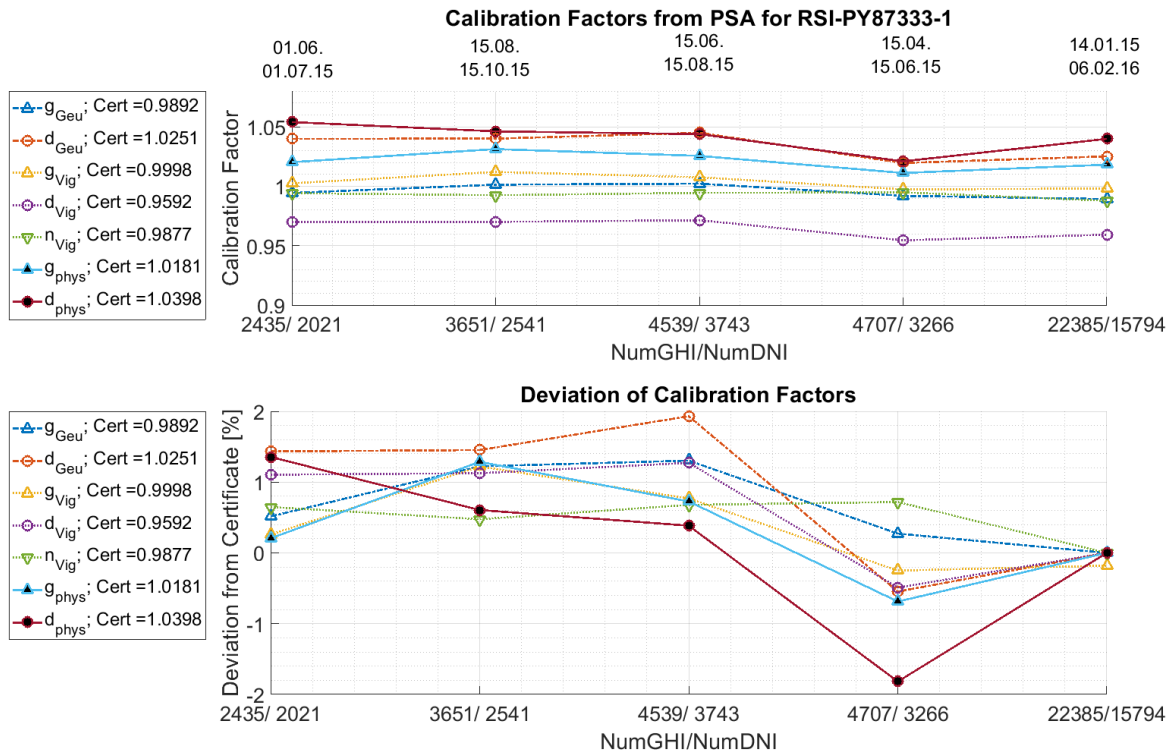


Figure 16: Calibration factors from calibrations at the PSA, Spain for different time ranges and their relative deviation with respect to the longest calibration time.

NumGHI is the number of used data points to calculate the g calibration factor and NumDNI is the number of used data points to calculate the d calibration factor, and n calibration factor in case of Vig. Cert is the calibration factor obtained from the longest calibration time range.

The variation of the calibration results from the physical calibration method (Phys) is comparable to the pre-existing calibration methods. A seasonal dependence of the calibration method cannot be observed. Expect for the time range from April 15th to June 15th, the deviation of the Phys calibration factors is less or equal to the deviation of the Geu calibration factors. Especially the deviation of the d calibration factor could be reduced significantly. This is particularly interesting because (Geuder et al., 2008) developed the calibration method with empirical relations from the PSA. The calibration method is therefore optimized for the climate at the PSA. Although no experimental data from the PSA is used to develop the new calibration function, the variation of the calibration factors can be reduced.

The observed deviation of the Phys calibration factor d_{phys} in the time range from April 15th to June 15th might stem from a significant number of days that are impacted by clouds in that time range. Especially then the Sedes2 model influences the spectral temperature correction of the time stamps and therefore the calibration results significantly. It has to be further investigated if the application of Sedes2 at the PSA results in an acceptable model of the cloud impacted spectra. However, the deviation of less than 2% for d_{phys} from the long term calibration is below the calibration uncertainty of 2.5% as stated for the Geu and Vig method by (Jessen, Wilbert, Nouri, Geuder, & Fritz, 2016). Furthermore, the corresponding

deviation in terms of DNI is for a deviation of less than 2% of the DHI much lower than for the GHI. The observed stability of the calibration factors is satisfying for all three methods.

The same sensor, which is calibrated above at the PSA (cf. Figure 16), is calibrated at NETRA as well, using an Aeronet station that is about 32km away and situated on a hill (Google Earth, 2018) (see also Appendix III on page 53). The used Aeronet data is of level 1.5, which is cloud cleared but is not fully quality assured (Aeronet, August 2018b). The time ranges vary between one and a half and nine months. It is worth pointing out that the time range of 1.5 months roughly compares to a calibration time of 1.5 weeks at the PSA and the time range of nine months roughly to two months at the PSA in terms of used data points. Most of the data points are sorted out because the sensors were not cleaned less than 24h before the measurement.

Figure 17 displays the calibration results and deviation of the calibration factors with respect to the longest calibration time at NETRA in the same manner as before in Figure 16 for the PSA.

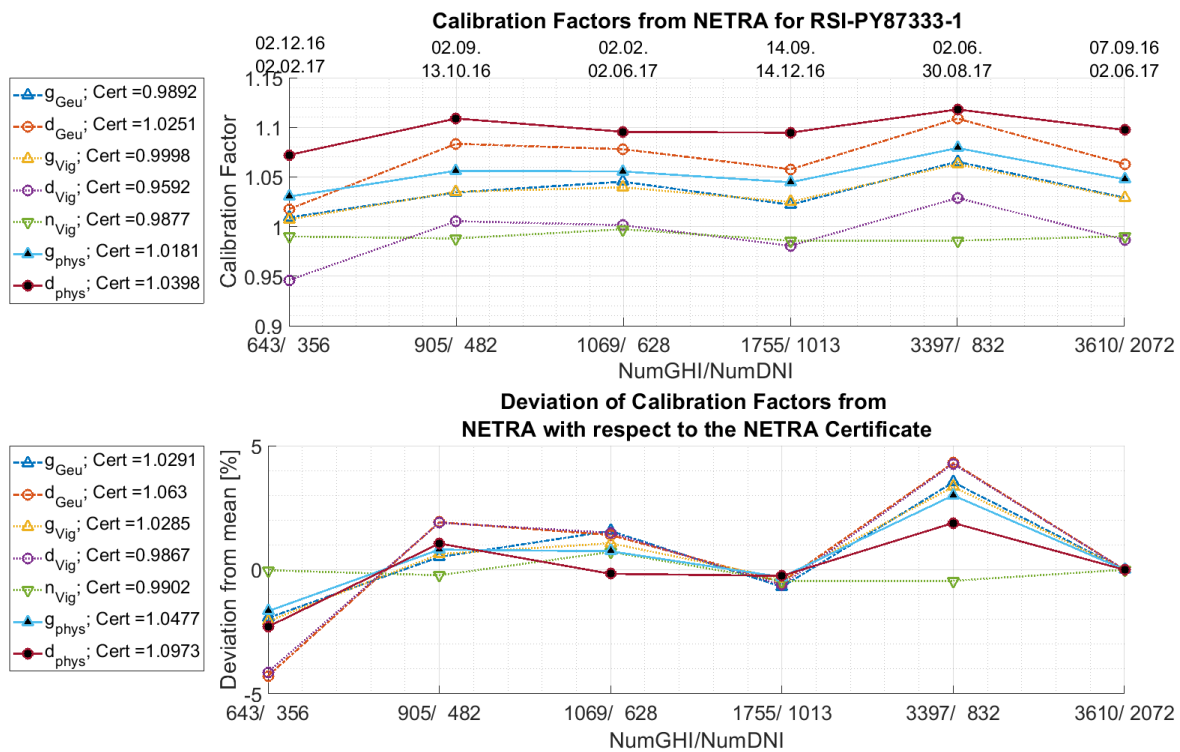


Figure 17: Calibration factors obtained at NETRA, India for different time ranges and calibration methods and their relative deviation with respect to the longest calibration time.

NumGHI is the number of used data points to calculate the g calibration factor and NumDNI is the number of used data points to calculate the d , and n in case of Vig, calibration factor. Cert is the respective calibration factor from the longest calibration time range.

The variation of the calibration factors in a warm temperature, winter dry, hot summer climate is stronger than at the PSA, but is reduced compared to Geu and Vig with the physical calibration method, especially for the d calibration factors. The deviation of both Phys calibration factors is below 3% for all

time ranges. This is still a quite high variation especially for the GHI, but a noticeable improvement compared to roughly 3.5% for Geu and Vig for the GHI and over 4% for the DHI. The largest deviation of the Phys calibration factors is observed from June 2nd to August 30th. This time range lies almost completely in summer monsoon in New Delhi (Wang & Ho, 2001). It is also questionable if the Sedes2 model can be applied as mentioned above. Since the applied filter allows all GHI measurements above $10 \frac{W}{m^2}$, the GHI calibration is most impacted by Sedes2. The d_{phys} calibration factor is only calculated with time stamps where the DNI is above $300 \frac{W}{m^2}$ because of the RMSD variation with respect to the DNI (cf. section 3.2). In the summer monsoon, there are few time stamps where this is the case. The calibration factor of the DHI is therefore not as affected by Sedes2. The application of Sedes2 at NETRA should be further investigated.

4.6 Summary

The correction results from NETRA, India show that the physical correction method is able to reduce the bias of the measurements for GHI, DHI and DNI significantly. Also, the RMSD is significantly reduced for the DHI and reduced for most cases of the experimental results for the GHI and DNI. At NETRA, the physical correction method is applied with quite a good estimation of the Angstrom exponents, single scattering albedo and asymmetry factor from a nearby Aeronet station. The used cloud checker is also optimized for the station at NETRA. It clearly shows the location dependence can be reduced with the physical correction method if the input parameters are well defined.

The correction results from Londrina show that the physical correction method has no real advantage if the assumptions about the atmosphere are too severe. Especially, the estimation of the aerosol type from an Aeronet station that is 550km away and the effect of the estimation of the pressure on the AOD has a significant effect on the uncertainties of the physical correction method. Another aspect is the cloud detection that is not optimized for this location. The results from NETRA suggest that with a better estimation of the input parameters, the correction results from Londrina might be improved.

Overall, the variation of the physical calibration factors at the PSA over the course of one year is better than the variation of Geuder. The relatively high deviation from the Cert of the Phys calibration factors in the spring could indicate that the physical calibration should be done only for days with little cloud presence. That way, the influence of the Sedes2 modification can be reduced. This should be investigated further. However, the physical method still reached a very good result considering that Geuder's method was developed at the PSA and was optimized for these climate conditions (Geuder et al., 2008). The variation of the calibration factors obtained at NETRA with the calibration interval is reduced when using the physical calibration method. Therefore, the seasonal dependence of the calibration factors is reduced by the physical calibration method compared to the pre-existing methods.

4.7 Room for improvement

The influence of the aerosols, the precipitable water vapor and the Sedes2 model can be considered to improve the physical correction method. This section only evaluates the influence of the aerosols and the precipitable water vapor.

An improvement in finding default values for the Angstroem exponents, single scattering albedo and asymmetry factors could improve the method's performance significantly. The aerosol type that is mainly present in the examined time range is then better estimated. The AOD calculation for long cloudy intervals could also be improved as the correction results from NETRA show for the monsoon time (cf. section 4.4.1). This might be achieved by using a default AOD value for cloudy conditions if the temporal closest AOD is too old.

The AOD at 550nm estimation with the Linke-Ineichen turbidity is a key component when correcting measurements with the physical correction method. The methods of calculating the AOD during the calibration and during the correction differ fundamentally (cf. sections 3.2 and 3.3). The following sections investigate, how well the iteration process during the physical correction (cf. section 3.3) estimates the AOD at 550nm. The estimation of the AOD depends on the calculated precipitable water vapor. How well the calculation of the precipitable water vapor by (Gueymard, 1993; Gueymard, 1995) fits the reference precipitable water vapor is also investigated. This analysis is done in the following two sections for the PSA and NETRA.

4.7.1 AOD and precipitable water vapor estimation at the PSA, Spain

The iteration process during the correction uses the calculated precipitable water vapor from (Gueymard, 1993; Gueymard, 1995) along Eq. (4) and an estimation of the AOD at 550nm (τ_{550nm}) along Eq. (7) by (Ineichen, 2008), which uses the current Linke-Ineichen turbidity, the precipitable water vapor and the current atmosphere pressure as input. The current Linke-Ineichen turbidity T_{LI} as stated, in Eq. (5) from (Ineichen & Perez, 2002), uses the altitude, the current DNI, the current distance between the earth and the sun and the altitude corrected air mass as input parameter.

The evaluation uses one year of data from the PSA and the following approach to evaluate the accuracy of the AOD estimation. First, the AOD at 550nm is estimated with the iteration process from the physical correction at the PSA over the course of one year for all sunny timestamps. The AOD at 550nm is also calculated from the measurement of α_2 and β from the Aeronet station along Eq. (3) as the most accurate reference. This is the AOD at 550nm that is used in the calibration method (cf. section 3.2). Then, the AOD at 550nm is calculated with reference measurements of the DNI from the pyrliometer and the precipitable water vapor from the Aeronet station. Because the physical correction calculates the water vapor with the equation given by (Gueymard, 1993; Gueymard, 1995), the AOD at 550nm is also calculated with the reference DNI and the calculated water vapor. All AOD at 550nm are compared to each other. The calculated precipitable water vapor is also compared to the measurement with the Aeronet station as a reference.

In Figure 19 and Figure 18 the results of the analysis are shown. On the y axis of Figure 19a) and Figure 18, the AOD at 550nm after the iteration process is displayed. This AOD is estimated during the correction process with the calculated precipitable water vapor and is only calculated for sunny time stamps. On the x axis of Figure 19a) and Figure 18 different reference AODs are shown. Figure 19b) shows the precipitable water vapor from the Aeronet station as the most accurate reference on the x axis and the calculated water vapor on the y axis. The color bar references how many measurement points fell into the corresponding pixels of the graphs.

First, it also needs to be investigated, how the estimated τ_{550nm} from the Linke-Ineichen turbidity along Eq. (7), fits the actual AOD at 550nm at the site as obtained by Aeronet measurements. The comparison between the τ_{550nm} after the iteration and the τ_{550nm} calculated from β and α_2 , measured with the Aeronet station is shown in Figure 18b). τ_{550nm} is calculated from β and α_2 using Eq. (3).

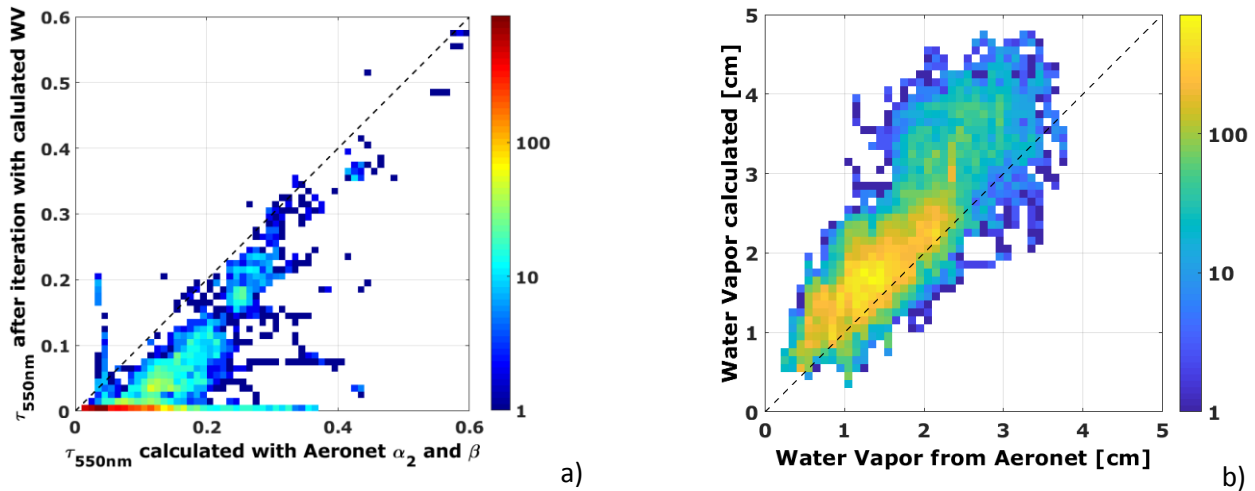


Figure 18: Evaluation of the AOD calculation by (Ineichen, 2008) and calculated precipitable water vapor by (Gueymard, 1993; Gueymard, 1995) for the PSA, Spain.

a) Calculated τ_{550nm} after the iteration process in comparison with τ_{550nm} calculated from Aeronet data for one year and sunny timestamps.

b) Calculated precipitable water vapor compared to measured water vapor from Aeronet measurements for one year.

The comparison in Figure 18a) clearly shows that the AOD after the iteration does not fit the actual AOD well for a lot of cases. The vertical and horizontal lines that can be observed in Figure 18a) are the effect of erroneous cloud filtering. The used cloud filter is optimized for the atmospheric conditions at NETRA so that some clouds at the PSA are not detected (Nouri, July 2018). Another effect that can be observed in Figure 18a) is the very dominant horizontal line at a very low τ_{550nm} after the iteration. For these cases the equation by (Ineichen, 2008) (cf. Eq. (7)) calculates negative AODs for the current Linke-Ineichen turbidity. These values are then automatically set to a low AOD of 0.00000001 by the physical correction method because SMARTS 2.9.5 expects a finite, positive AOD as input parameter.

The described effects are problematic because during the calibration, β is used to simulate the spectra with SMARTS 2.9.5 and during the correction, the calculated τ_{550nm} from (Ineichen, 2008) is used. There are a number of possible reasons why the differences can be observed. For one, the function to obtain τ_{550nm} from the T_U by (Ineichen, 2008) uses an urban aerosol type. This is a poor choice for the remote PSA in a more rural environment and only about 40km away from the coast (Google Earth, 2018). The SMARTS 2.9.5 simulation software converts by default the turbidity input parameters to β along Eq. (3). This has a huge impact in the correction method because the α_2 , which is given to SMARTS 2.9.5 during the correction process, is a default value obtained from an average from a selected year. Obviously, this value does not reflect the current α_2 at the measurement site at all times. This stresses the importance of correct estimations of the Angstrom exponents prior to the correction at a site.

Figure 18b) shows that the calculated precipitable water vapor is too high in comparison with the reference precipitable water vapor from Aeronet. The influence of the calculation of precipitable water vapor on the AOD at 550nm is therefore investigated in Figure 19a) and b).

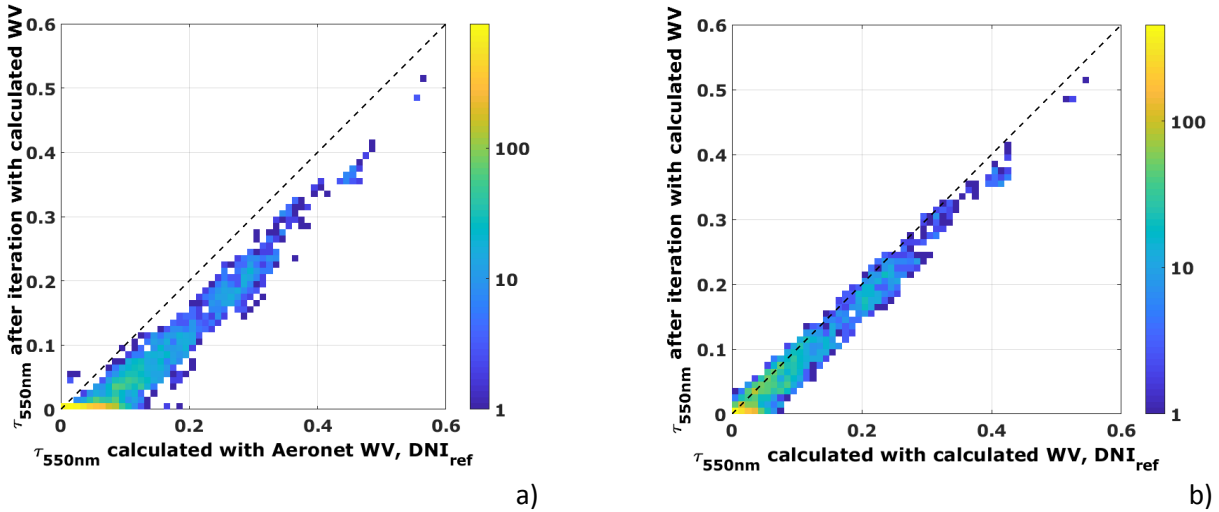


Figure 19: Evaluation of τ_{550nm} for sunny time stamps over the course of one year at the PSA
a) Calculated τ_{550nm} after the iteration process in comparison with the τ_{550nm} calculated with Aeronet precipitable water vapor and the reference DNI.
b) Calculated τ_{550nm} after the iteration process in comparison with τ_{550nm} calculated with the calculated precipitable water vapor and the reference DNI.

The resulting τ_{550nm} for all sunny time stamps from iteration process of the correction method is compared to the τ_{550nm} calculated from the measured precipitable water vapor from Aeronet and the reference DNI from the pyrliometer (c. f. Figure 19a) and the τ_{550nm} calculated from the calculated water vapor and the reference DNI from the pyrliometer (c. f. Figure 19b).

Figure 19a) and b) clearly show the influence of the source of the precipitable water vapor on the calculation of the AOD. Figure 19a) suggests that the iteration process does not estimate the AOD well because the AOD is estimated too low. The bias that can be observed in Figure 19a) can be explained by the bias of the water vapor calculation (cf. Figure 18b). A higher precipitable water vapor leads to a smaller estimated AOD. When evaluating Figures 19b) it becomes apparent that the AOD after the iteration process shows a smaller bias when the reference AOD is also calculated with the calculated water vapor. It should therefore be investigated if the formula to calculate the precipitable water vapor can be adapted to the PSA, Spain.

It also needs to be investigated how the iteration process changes the estimated AOD for the sunny time stamps. This comparison is shown in Figure 20.

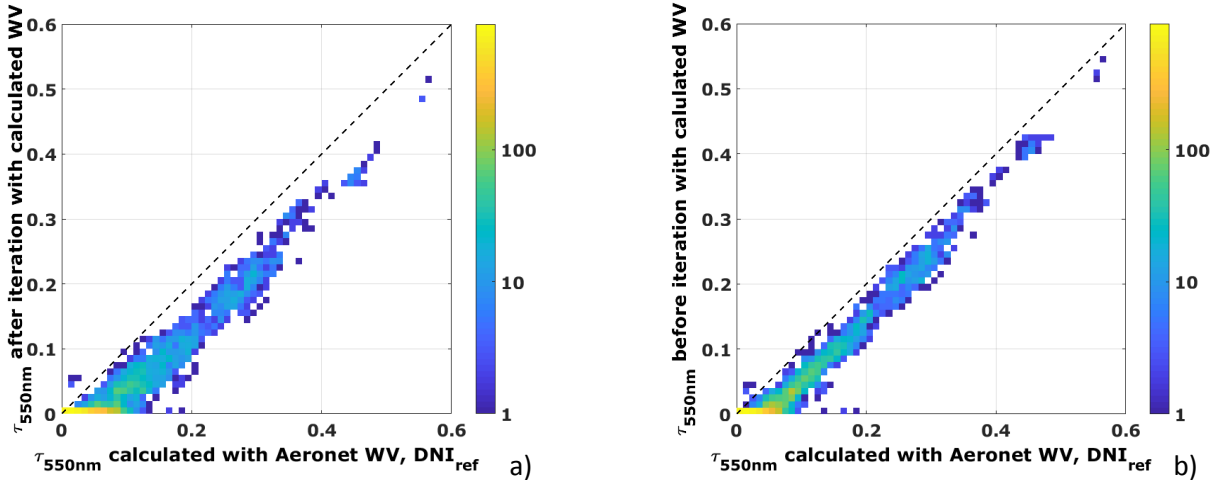


Figure 20: Evaluation of τ_{550nm} for sunny time stamps before and after the iteration at the PSA

a) Calculated τ_{550nm} after the iteration process in comparison with the τ_{550nm} calculated with Aeronet precipitable water vapor and the reference DNI.

b) Calculated τ_{550nm} before the iteration process in comparison with the τ_{550nm} calculated with Aeronet precipitable water vapor and the reference DNI.

When comparing the two obtained τ_{550nm} before and after the iteration to the calculated τ_{550nm} with the Linke-Ineichen turbidity obtained from reference sensors and the calculated precipitable water vapor in Figure 20, one notices that the iteration seems to increase the standard deviation of the calculated τ_{550nm} and the underestimation of τ_{550nm} . A possible explanation is that the aerosol type used to calculate τ_{550nm} with the Linke-Ineichen turbidity does not match the Angstrom exponents that are used in the SMARTS 2.9.5 calculation during the iteration process. The break condition used in the iteration is a small change of the spectral temperature correction factor, which ensures self-consistency of the correction results. However, this cannot guarantee that the obtained factors are actually correct. The relationship between τ_{550nm} and the selected Angstrom exponents needs to be investigated further and possibly an adjustment of the break condition of the iteration process might be considered.

Another possible solution for the problems discussed before might be a calibration that is closer to the actual correction method. That way, the atmosphere during the calibration is not estimated with the best possible measurements, but the influence of the calculation of precipitable water vapor and the calculation of the AOD with the Linke-Ineichen turbidity might be reduced if the deviations caused by the estimation are similar at the calibration test site. The result could be calibration factors that fit the correction better and therefore might result in better correction results. Also, the calibration could then also be less dependent of a nearby Aeronet station.

4.7.2 AOD and precipitable water vapor estimation at NETRA, India

The same investigation as in section 4.7.1 above is done for NETRA, India using Aeronet data from Gual Pahari. Note, that even though the investigation is done for one year as well, there are far less data points in Figure 22 and Figure 21a) then in Figure 19 and Figure 18. Reasons for that difference are the premise that the investigation for NETRA is only done for sunny time stamps and clean reference

sensors. Because of the fewer data points such a thorough investigation as done for the PSA is not possible for NETRA.

Figure 21a) shows the comparison between the τ_{550nm} obtained from the iteration process and the calculated τ_{550nm} from the Aeronet β and α_2 at Gual Pahari. The sample size is much smaller than for the comparison done in Figure 18a) at the PSA.

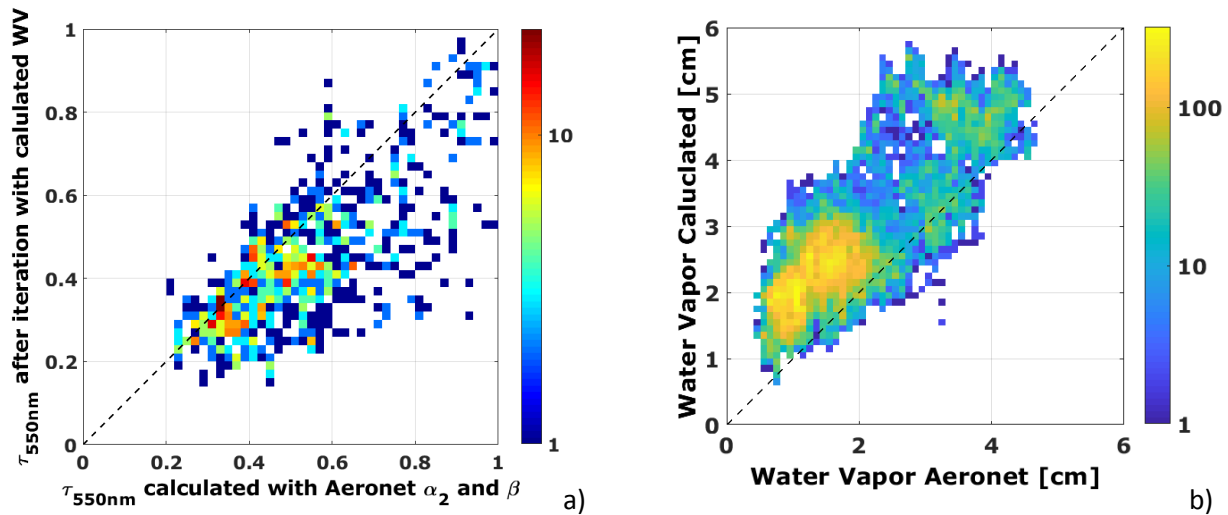


Figure 21: Evaluation of the AOD calculated by (Ineichen, 2008) and calculated precipitable water vapor by (Gueymard, 1993; Gueymard, 1995) for NETRA.

a) Calculated τ_{550nm} after the iteration process with τ_{550nm} calculated from Aeronet data from Gual Pahari.

b) Calculated precipitable water vapor at NETRA compared to precipitable measured water vapor at Gual Pahari.

The τ_{550nm} after the iteration does not show a significant bias, but the deviations between the reference AOD obtained with Aeronet and the AOD after the iteration are much higher than at the PSA. The spreading of the AOD values could be explained by the different locations of the stations. The τ_{550nm} on the vertical axis is calculated only with input parameters from NETRA while the τ_{550nm} on the horizontal axis is calculated solely from the Aeronet measurements at Gual Pahari. The NETRA station lays directly in the wind direction coming from New Delhi. The aerosols in the atmosphere above NETRA might therefore be different than the aerosols present at Gual Pahari. If the wind direction is the same for Gual Pahari as it is for NETRA, the aerosols above Gual Pahari are rather mixed with the aerosols coming from the surroundings of New Delhi (see also the map in Appendix III on page 53).

The comparison in Figure 21b) between the calculated precipitable water vapor from ambient temperature, relative humidity and pressure, measured at NETRA with the formula provided by (Gueymard, 1993; Gueymard, 1995) and the precipitable water vapor as measured at the Aeronet site in Gual Pahari shows that the water vapor is clearly estimated too high. One reason could be the distance between the NETRA and Gual Pahari stations. The Aeronet station is situated about 50 meters above the NETRA station and is about 32km away (Google Earth, 2018) (see also the map in Appendix II.). Another possible explanation could be that the formula itself calculates the precipitable water vapor too high

because the calculation of the precipitable water vapor at the PSA, Spain is also calculated too high (c. f. Figure 18a). The result itself does not imply that the formula to calculate the precipitable water vapor is not applicable at NETRA. A further study should be conducted with a reference station measuring relative humidity and ambient temperature next to the Aeronet station. For a quantitative statement, more data from different locations is needed.

Figure 22 shows the AOD after the iteration in comparison with the AOD calculated from the reference DNI from the pyrheliometer at NETRA and either the precipitable water vapor from the Aeronet station at Gual Pahari (Figure 22a) or the calculated precipitable water vapor (Figure 22b).

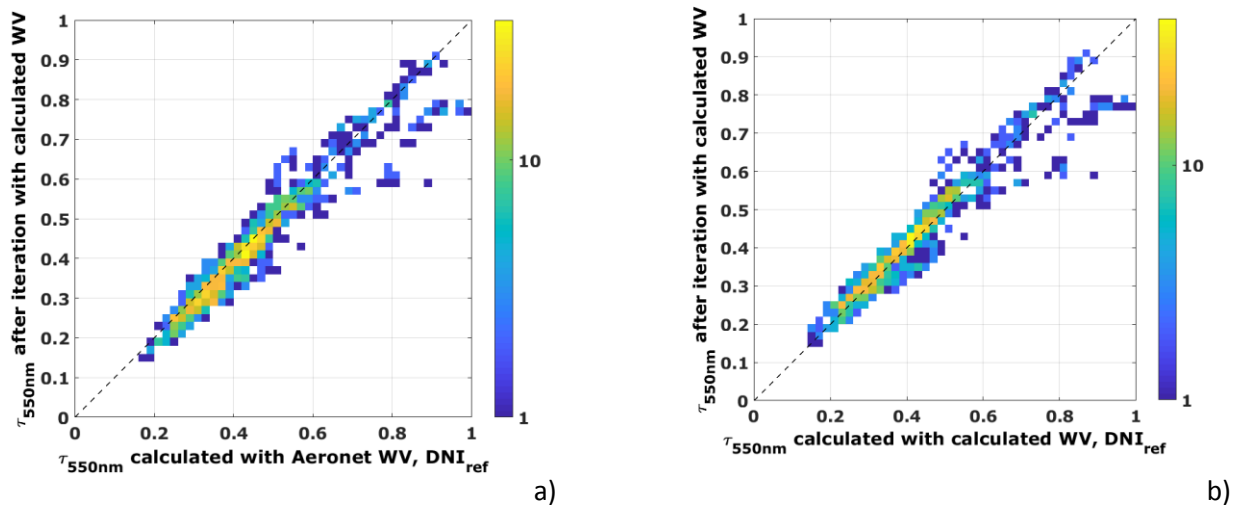


Figure 22: Evaluation of τ_{550nm} for sunny time stamps over the course of one year at NETRA
a) Calculated τ_{550nm} after the iteration process in comparison with the τ_{550nm} calculated with Aeronet precipitable water vapor from Gual Pahari and the reference DNI.
b) Calculated τ_{550nm} after the iteration process in comparison with τ_{550nm} calculated with the calculated precipitable water vapor and the reference DNI.

First of all, the comparison between Figure 22a) and b) shows that the estimation with the iteration process works better at NETRA than at the PSA (cf. Figure 19). A small bias can be observed when comparing the τ_{550nm} after the iteration with the τ_{550nm} calculated with the precipitable water vapor measured at the Aeronet station at Gual Pahari. This bias can also be observed in Figure 21a). An analysis of the effect of the iteration process AOD, similar to Figure 20, is done for NETRA as well and revealed that the standard deviation of the AOD is also slightly increased after the iteration. The underestimation that is apparent at the PSA (cf. Figure 20) could not be observed at NETRA.

4.7.3 Summary of the options to improve the physical methods

All in all, this investigation shows that there is room for improvement for the correction method. The τ_{550nm} that is calculated during the correction is converted by SMARTS 2.9.5 to β using the default α_2 . This cannot represent the current value for most time stamps. It should be investigated if it is possible to directly estimate β better from atmospheric parameters or if better results are achieved with a default aerosol type. It should also be investigated if the calculation of the AOD at 550nm with (Ineichen, 2008) is only applicable for urban aerosol types and better estimation results at the PSA are achieved if a rural

aerosol type is used for obtaining the conversion formula. The calculation of the precipitable water vapor by (Gueymard, 1993; Gueymard, 1995) also needs to be reviewed and possibly adjusted, especially for the PSA, Spain.

The calibration and correction methods might also benefit, if the calibration is done with calculated precipitable water vapor along Eq. (4) and the AOD is calculated with the reference DNI and the calculated water vapor as opposed to the Aeronet input. That way, the calibration method is less dependent on a nearby Aeronet station and the calibration is closer to the actual correction method. This could lead to calibration factors that might fit the measurements and their correction better because the difference between the precipitable water vapor calculation and AOD in the two methods is then less dominant.

5 Conclusion and Outlook

A new calibration and correction method for RSIs based on physical principals has been developed. The spectral temperature correction corresponds to the broadband corrections that were derived so far by Geuder and King. Differences between the so far used broadband temperature corrections can be explained and reproduced by using the different spectra that were most likely present during the experimental determination of the broadband temperature corrections. The newly found cosine correction function can be applied as a standalone function to the DNI as opposed to the current correction sets where the empirical correction functions for the cosine and spectral effects of the calibration factors are intervened and only applicable to the GHI.

The physical correction method shows good results in regards of reducing the location dependence, especially in the previously problematic case of the NETRA station. That way, the here presented set of calibration and correction functions can be applied under very different climate conditions. The physical correction method works well in removing the bias from the measurements of GHI, DHI and DNI and can reduce the RMSD most of the time, especially for the DHI component.

The seasonal variation of the calibration factors obtained at one station is also significantly reduced by the new physical calibration function. Even at the PSA, where the calibration function by Geuder was developed, the physical calibration factors show less variation over the course of one year. In the humid climate of the NETRA station, the variation of the calibration factors can also be reduced by the new calibration method in comparison with the variation of the Vignola and Geuder calibration factors.

Correction results from Londrina, Brazil show that the determination of the input parameters can still be improved. Better results might be possible with improved estimations of aerosol type and an improved cloud checker. Especially the results from NETRA show the importance of a good estimation of the input parameters and cloud detection because the good results there are achieved with quite rudimentary assumptions about the aerosol properties from an Aeronet station near-by. An investigation to further improve the aerosol input parameters should therefore be done.

The application of the enhanced Sedes2 model on the GHI instead of the GTI also seems to introduce significant errors. Especially the application of Sedes2 at the different stations needs to be further

investigated. An improved model could easily be included in the physical correction and calibration function.

Calculating the precipitable water vapor from the ambient temperature and relative humidity at the correction site induces a significant bias in the calculation of the aerosol optical depth. Especially for the PSA, Spain, the calculation needs to be reviewed and possibly adjusted.

The iteration process of the correction method currently underestimates the AOD. One explanation can be the overestimation of precipitable water vapor by the used formula. Also, the calculated AOD during the iteration is automatically converted to the Angstroem turbidity by SMARTS 2.9.5. It uses the quite rudimentary input parameters for this conversion and it should therefore be investigated if the Angstroem turbidity can be better estimated directly from the atmospheric parameters available at the measurement site of the RSI. The used iteration process also seems to increase the standard deviation of the AOD during the iteration process. It should therefore be investigated if the estimation of the AOD with the Linke-Ineichen turbidity is applicable for non-urban aerosol types.

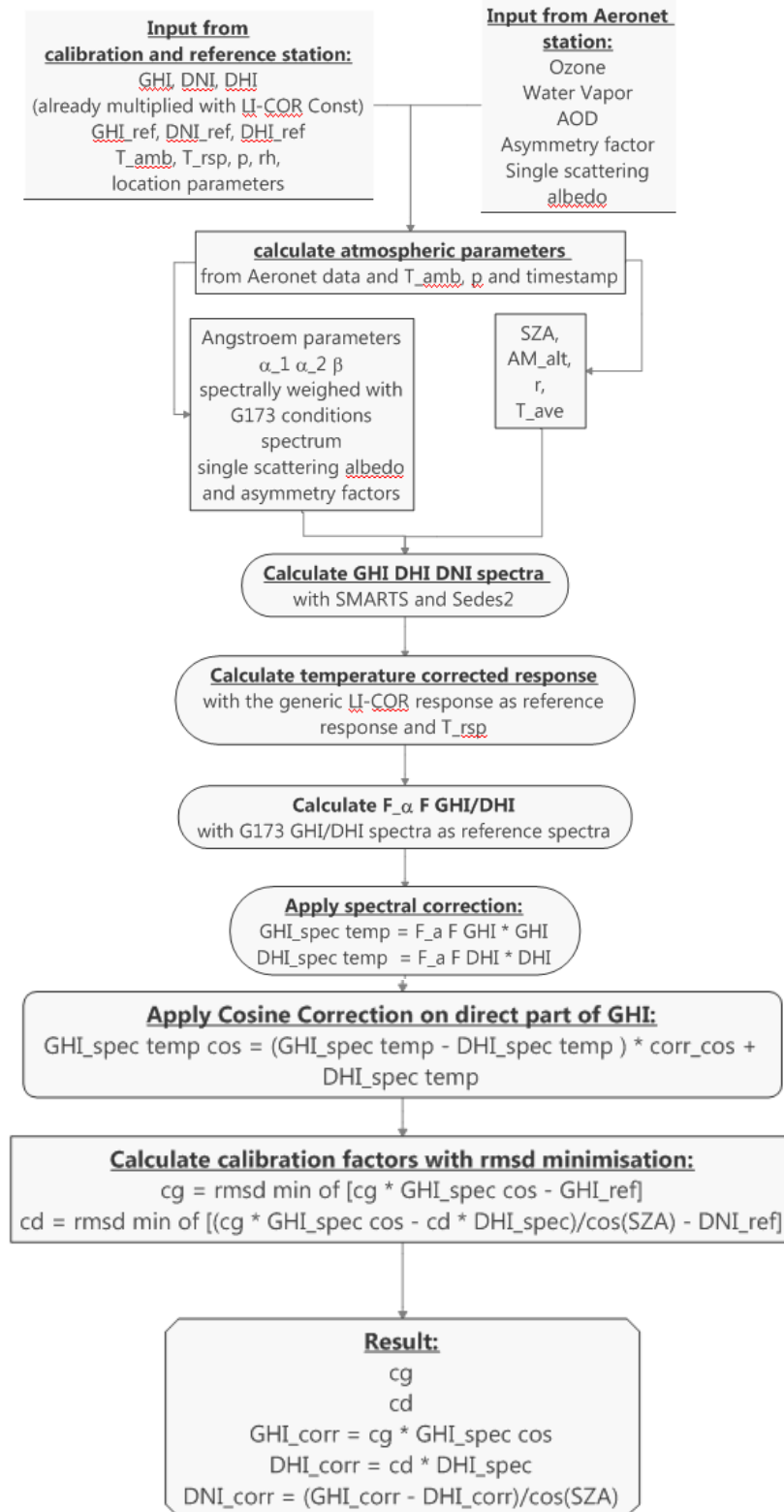
For stations that are far away from any Aeronet station where the estimation aerosol type from an Aeronet station is questionable, a solution might be the use of default aerosol types that are already implemented in SMARTS 2.9.5. This should be further investigated especially at Londrina, Brazil.

The interplay of the calibration and correction function might also be improved with the premise, that the atmosphere during the calibration is not estimated with the best available input parameters, but also with calculation of the AOD with the Ineichen-turbidity and the calculated precipitable water vapor from the relative humidity and ambient temperature. An advantage might be that the calibration function and the correction function are more similar in estimating the atmosphere around the sensor and therefore the calibration factors fit the correction method better.

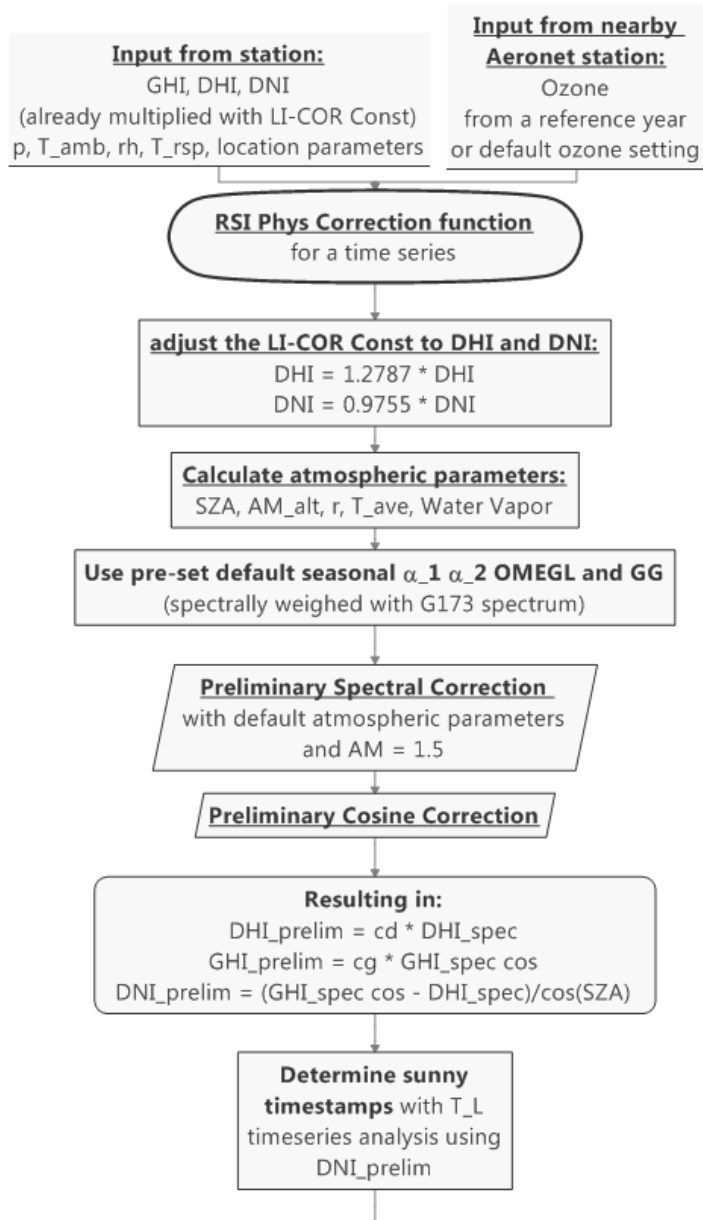
In conclusion, the physical calibration and correction methods are able to reduce the problematic location dependence of the pre-existing calibration and correction methods by Geuder and Vignola. More stations at different locations should be examined to further examine the results achieved by the physical correction. The physical correction and calibration methods show promising results for a further improvement of the RSI accuracy. Even better results could be achieved with an improvement of the AOD estimation, the precipitable water vapor calculation and the handling of clouds.

Appendix

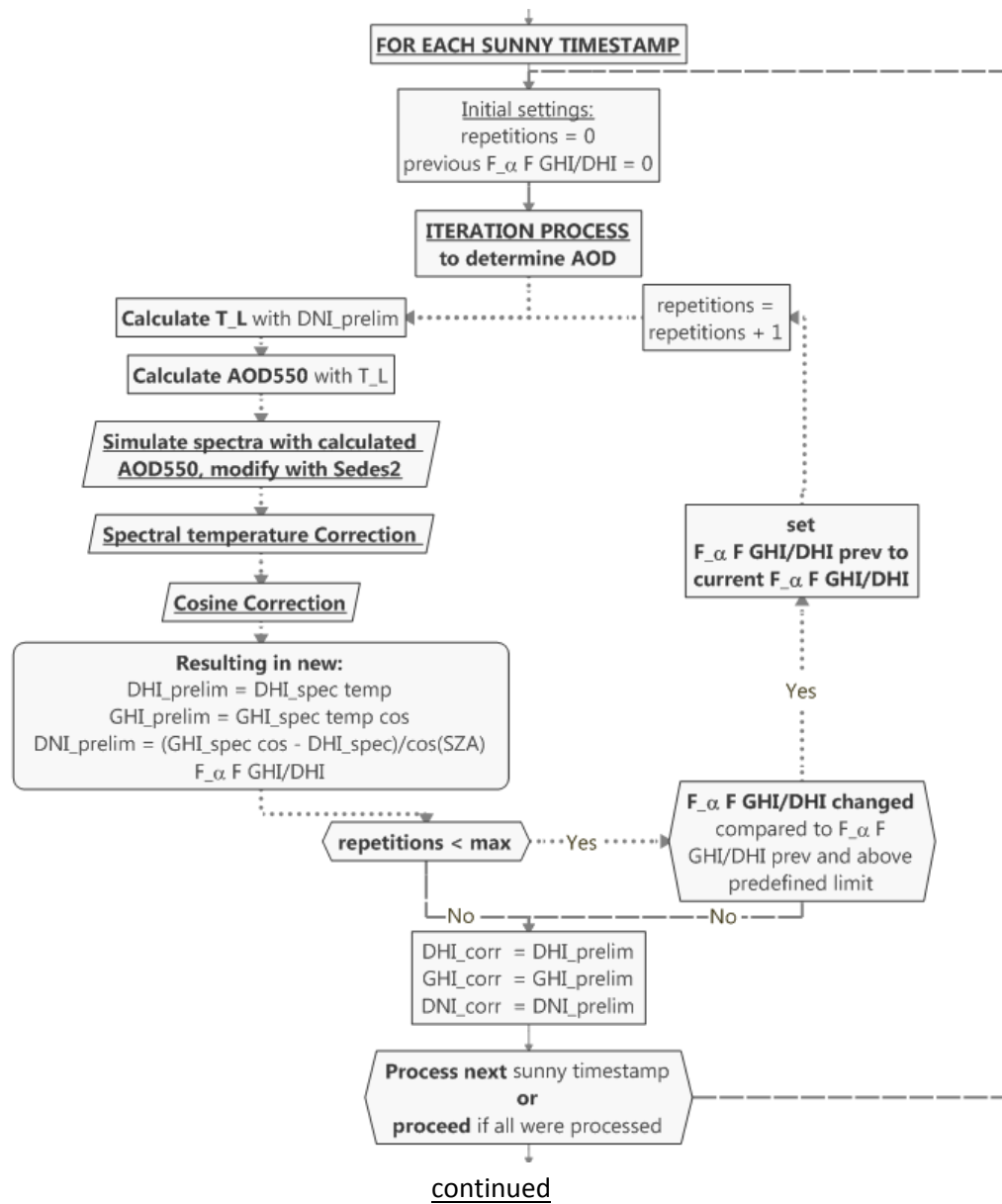
I. Flowchart of the calibration method:

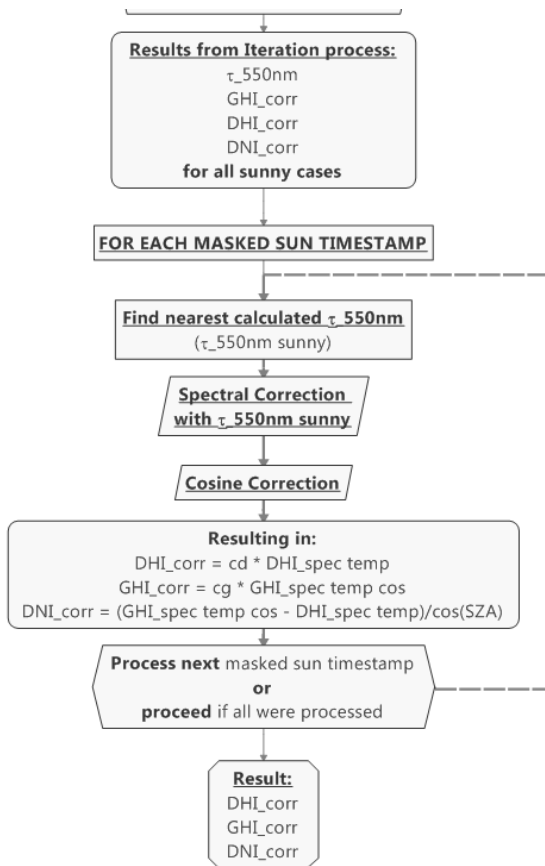


II. Flowchart of the correction method:



continued

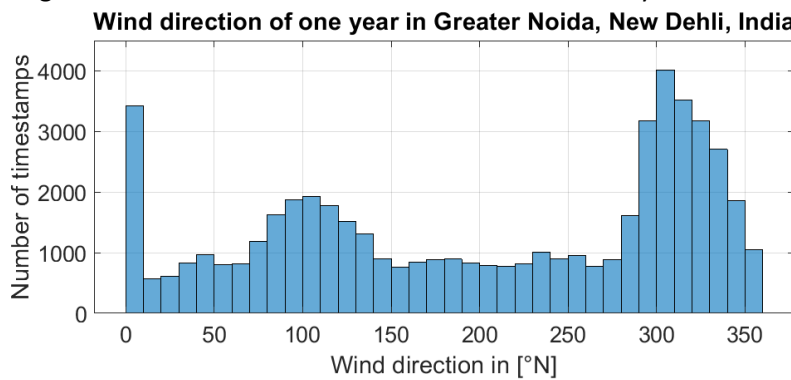




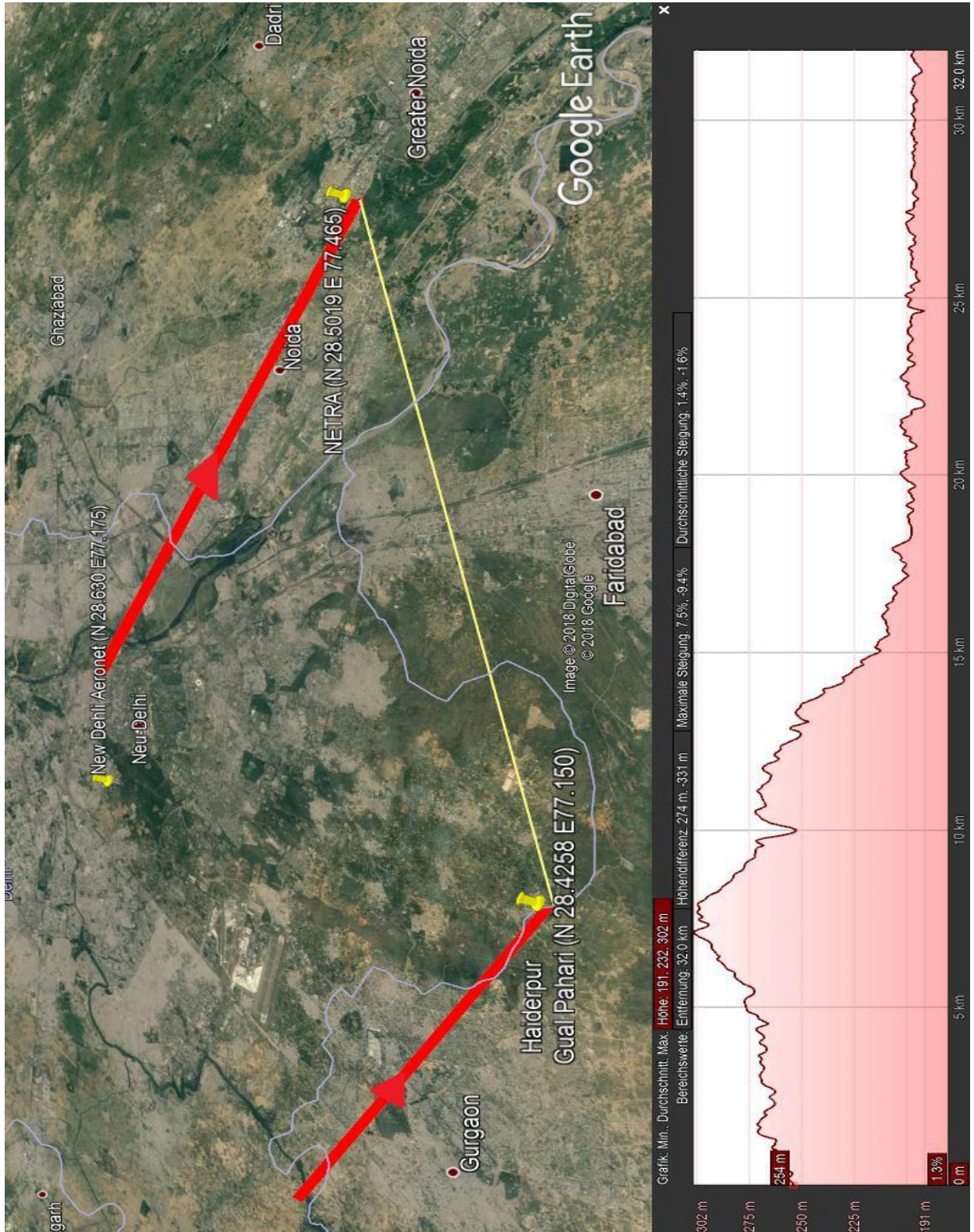
The results are for all processed time stamps.

III. Site evaluation of NETRA

Histogram of the wind direction over the course of one year at NETRA, bin size 10°:

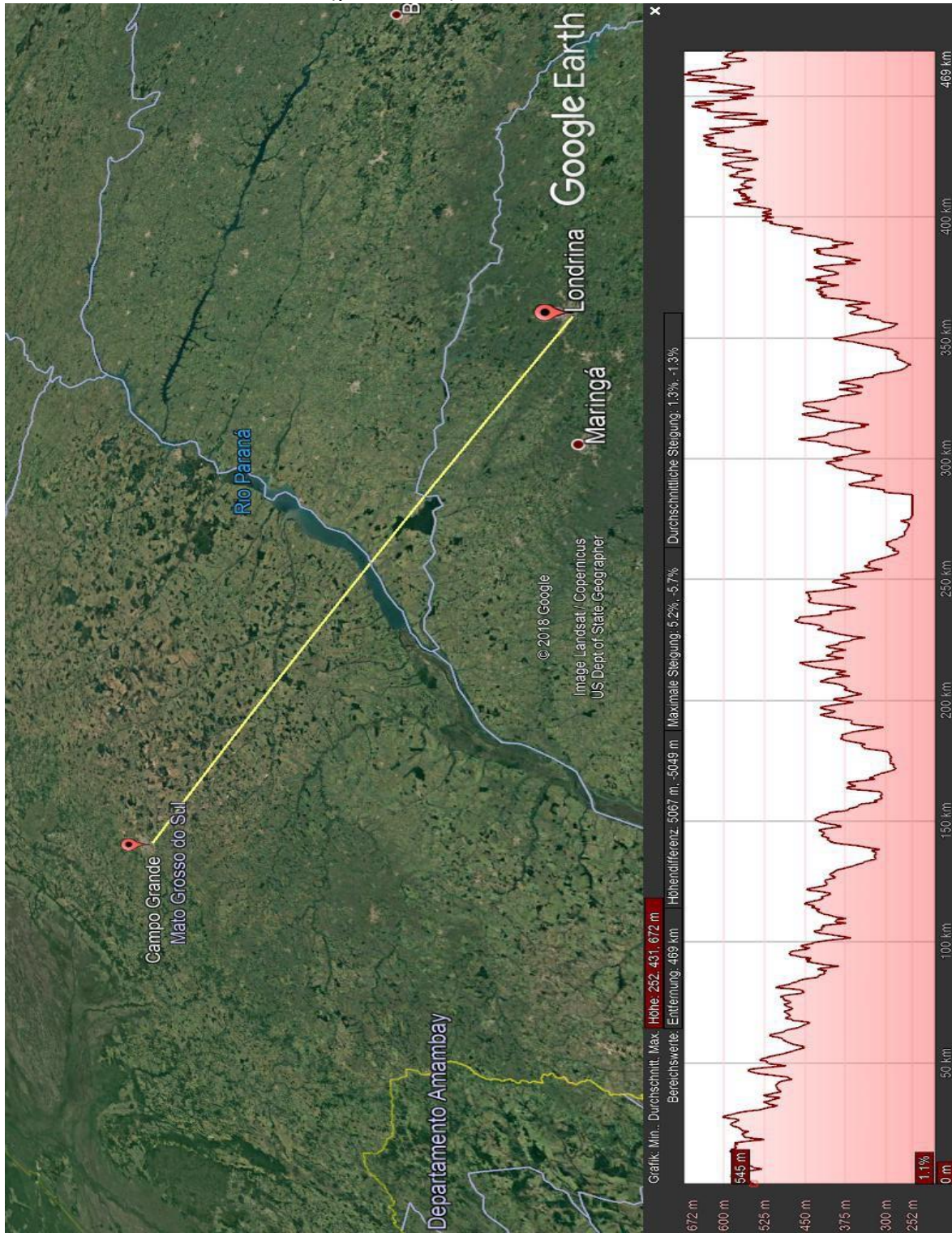


The distance and height profile between the Aeronet station in Gual Pahari and NETRA. The thick line marks the main wind direction (305°) as measured at NETRA. It references from where the wind is blowing with thick arrows. The distance (yellow line) is measured as 32.0km.



IV. Londrina

The distance and height profile between the Aeronet station in Campo Grande and Londrina. The distance (yellow line) is measured to be 469km.



References

- Aeronet. August 2018a. Site Campo Grande SONDA, https://aeronet.gsfc.nasa.gov/cgi-bin/type_one_station_opera_v2_new?site=Campo_Grande_SONDA&nachal=0&year=25&aero_water=0&if_day=0&year_or_month=1&level=2&place_code=10. Last visited 31. Aug. 2018.
- Aeronet. August 2018b. Site Gual Pahari, https://aeronet.gsfc.nasa.gov/cgi-bin/type_one_station_opera_v2_new?site=Gual_Pahari&nachal=0&year=16&aero_water=0&level=2&if_day=0&if_err=0&place_code=10&year_or_month=1. Last visited 31. Aug. 2018.
- Aeronet. August 2018c. Site New Dehli, https://aeronet.gsfc.nasa.gov/cgi-bin/type_one_station_opera_v2_new?site=New_Delhi&nachal=2&level=3&place_code=10. Last visited 31. Aug. 2018.
- Aeronet. August 2018d. Site Tabernas PSA DLR, https://aeronet.gsfc.nasa.gov/cgi-bin/type_one_station_opera_v2_new?site=Tabernas_PSA-DLR&nachal=2&level=2&place_code=10. Last visited 31. Aug. 2018.
- ASTM, G173-03. 2012. Standard Tables for Reference Solar Spectral Irradiances, *Direct Normal and Hemispherical on 37° Tilted Surface*. ASTM: ASTM International.
- ASTM, G214-15. 2016. Standard Test Method for Intergration of Digital Spectral Data for Weathering and Durability Applications, Vol. G214-15. ASTM: ASTM International.
- Augustyn, J., Geer, T., Stoffel, T., Vignola, F., Kessler, R., Kern, E., Little, R., & Boyson, B. 2004. Update of Algorithm to Correct Direct Normal Irradiance Measurements Made with a Rotating Shadow Band Pyranometer, *Solar 2004 Conference*: 295-302. Portland, OR: American Solar Energy Soc.
- Bludau, W. 1974. Temperature dependence of the band gap of silicon. *Journal of Applied Physics*, 45(1846).
- CSP Services. August 2018, <http://www.cspservices.de/products-services/measurement-systems/mdi>. Last visited 31. Aug. 2018.
- DLR. 2018. Meteorological Database. In Q. T. German Aerospace Center Institute of Solar Research, Spain (Ed.).
- Geuder, N., Pulvermüller, B., & Vorbrugg, O. 2008. Corrections for rotating shadowband pyranometers for solar resource assessment, *Solar Energy + Applications*. San Diego, USA: Proceedings of SPIE 70460, International Society for Optical Engineering, Society of Photo-Optical Instrumentation Engineers.
- Geuder, N., Pulvermüller, B., et. al.,. 2008. Original Data set from N. Geuder, reviewed with S. Wilbert in July 2018: German Aerospace Center Institute of Solar Research, Qualification Tabernas, Spain.
- Geuder, N., Wolfertstetter, F., Wilbert, S., Schüler, D., Affolter, R., Kraas, B., Lüpfer, E., & Espinar, B. 2015. Screening and Flagging of Solar Irradiation and Ancillary Meteorological Data. *Energy Procedia*, 69(0): 1989-1998.
- Google Earth. 2018. Google Earth Pro Version 7.3.1 Desktop Version.
- Gueymard, C. 1993. Assessment of the accuracy and computing speed of simplified saturation vapor equations using a new reference dataset. *Journal of Applied Meteorology*, 32(7): 1294-1300.
- Gueymard, C. 1994. Analysis of monthly average atmospheric precipitable water and turbidity in Canada and Northern United States. *Solar Energy*, 53(1): 57-71.
- Gueymard, C. 1995. SMARTS2, a simple model of the atmospheric radiative transfer of sunshine: algorithms and performance assessment. Rep. FSEC-PF-270-95
- Gueymard, C. 2001. Parameterized transmittance model for direct beam and circumsolar spectral irradiance. *Solar Energy*, 71(5): 325-346.
- Gueymard, C. A. 2005. SMARTS code, version 2.9.5. *USER'S MANUAL For Windows*.

- Hishikawa, Y., Yoshita, M., Ohshima, H., Yamagoe, K., Shimura, H., Sasaki, A., & Ueda, T. 2018. Temperature dependence of the short circuit current and spectral responsivity of various kinds of crystalline silicon photovoltaic devices. *Japanese Journal of Applied Physics*, 57(08RG17).
- Ineichen, P. 2008. Conversion function between the Linke turbidity and the atmospheric water vapor and aerosol content. *Solar Energy*, 82(11): 1095-1097.
- Ineichen, P., & Perez, R. 2002. A new airmass independent formulation for the Linke turbidity coefficient. *Solar Energy*, 73(3): 151-157.
- Jessen, W., Wilbert, S., Gueymard, C. A., Polo, J., Bian, Z., Driesse, A., Habte, A., Marzo, A., Armstrong, P. R., Vignola, F., & Ramírez, L. 2018. Proposal and evaluation of subordinate standard solar irradiance spectra for applications in solar energy systems. *Solar Energy*, 168: 30-43.
- Jessen, W., Wilbert, S., Nouri, B., Geuder, N., & Fritz, H. 2016. Calibration methods for rotating shadowband irradiometers and optimizing the calibration duration. *Atmos. Meas. Tech.*, 9(4): 1601-1612.
- Jessen, W., Wilbert, S., Zarzalejo Tirado, L., Ramirez Santigosa, L., Valenzuela Balderrama, R., Liria, J., Nouri, B., & Hanrieder, N. 2017. Calibration Procedures for Rotating Shadowband Irradiometers. *SFERA II*.
- Kasten, F., & Young, A. T. 1989. Revised optical air mass tables and approximation formula. *Applied Optics*, 28(22): 4735-4738.
- King-Smith, R. D. 1989. A First-Principle Calculation of the Temperature Dependence of the Indirect Band Gap of Silicon. *Europhysics Letters*, 10(6): 569-574.
- King, D. L., & Myers, D. R. 1997. Silicon-photodiode pyranometers: Operational characteristics, historical experiences, and new calibration procedures, *Photovoltaic Specialists Conference*: 1285-1288: IEEE.
- Klingshirn, C. F. 2006. 3.2 Microscopic Aspects, *Semiconductor Optics*, 3 ed., Vol. Ed. 3, ISBN 3-540-21328-7: 65ff: Springer.
- Kottek, M. 2005. World Map of the Köppen-Geiger climate classification updated *Meteorologische Zeitschrift*, 15(3): 259-263.
- Licor. 2004. Radiation measurement Instruments: LI-COR Biosciences. Meteorology Group. August 2018. Internal source code.
- Michalsky, J. J. 1988. The Astronomical Almanac's algorithm for approximate solar position (1950-2050). *Solar Energy*, 40(3): 227-235.
- Myers, D. R. 2012. Direct beam and hemispherical terrestrial solar spectral distributions derived from broadband hourly solar radiation data. *Solar Energy*, 86(2771-2782).
- Nann, S., & Riordan, C. 1991. Solar spectral irradiance under clear and cloudy skies: Measurements and a semiempirical model. *Journal of Applied Meteorology*, 30(4): 447-462.
- NASA. August 2018. <https://aeronet.gsfc.nasa.gov/>. Last visited 31. Aug. 2018.
- Nouri, B. July 2018. Personal communication. German Aerospace Center Institute of Solar Research, Qualification Tabernas, Spain.
- Olsen, S. C., & Randerson, J. T. 2004. Differences between surface and column atmospheric CO₂ and implications for carbon cycle research. *Journal of Geophysical Research*, 109(D02301).
- Rajkanan, K., Singh, R., & Shewchun, J. 1979. Absorption coefficient of silicon for solar cell calculations. *Solid-State Electronics*, 22: 793-795.
- S. Nann, C. R. 1990. Solar Spectral Irradiance Under Overcast Skies, *21st IEEE Photovoltaic Specialists Conference*. Orlando.
- Varshni, Y. P. 1967. Band-to-Band Radiative Recombination in Groups IV, VI, and III-V Semiconductors. *Physica (phys. stat. sol)*, 19(459).
- Vignola, F. 2006. Removing Systematic Errors from Rotating Shadowband Pyranometer Data. *Proceedings American Solar Energy Society*.

- Vignola, F., Derocher, Z., Peterson, J., Vuilleumier, L., Félix, C., Gröbner, J., & Kouremeti, N. 2016. Effects of changing spectral radiation distribution on the performance of photodiode pyranometers. *Solar Energy*, 129: 224-235.
- Vignola, F., Peterson, J., Mavromatakis, F., Wilbert, S., Forstinger, A., Dooraghi, M., & Sengupta, M. 2018. Removing Biases from Rotating Shadowband Radiometers. *Solar Paces*, currently under review, submitted 24.08.2018.
- Wang, B., & Ho, L. 2001. Rainy season of the Asian-Pacific Summer Monsoon. *Journal of Climate*, 15: 386-398.
- Wikipedia. August 2018a. Campo Grande, https://en.wikipedia.org/wiki/Campo_Grande. Last visited 31. Aug. 2018.
- Wikipedia. August 2018b. Londrina, <https://en.wikipedia.org/wiki/Londrina>. Last visited 31. Aug. 2018.
- Wilbert, S. 2014. *Determination of Circumsolar Radiation and its Effect on Concentrating Solar Power*. Published PhD thesis, Rheinisch-Westfälische Technische Hochschule Aachen, DLR.
- Wilbert, S., Geuder, N., Schwandt, M., Kraas, B., Jessen, W., Meyer, R., & Nouri, B. 2015. Best Practices for Solar Irradiance Measurements with Rotating Shadowband Irradiometers. International Energy Agency; Solar Heating & Cooling Programme.
- Wilcox, S., & Marion, W. 2008. *Users manual for TMY3 data sets*: National Renewable Energy Laboratory Golden, CO.
- Wilko Jessen, S. W., Christian Gueymard, Jesús Polo, Zeqiang Bian, Anton Driesse, Aron Habte, Aitor Marzo, Peter Armstrong, Frank Vignola, Lourdes Ramírez. 2017. Proposal and Evaluation of Subordinate Standard Solar Irradiance Spectra for Applications in Solar Energy Systems. *Solar Energy*.
- WMO. 2014. *Guide to Meteorological Instruments and Methods of Observation*. WMO-No. 8, 2014 Update. (Eighth ed.).